

Geochemistry, Geophysics, Geosystems

RESEARCH ARTICLE

10.1002/2014GC005589

Key Points:

- 2006 eruption at Augustine brought to the surface dioritic inclusions with zircon dated at 26 ka
- Late Pleistocene rhyolite fall deposit also has zircon interiors and rims with ages of \sim 26 ka
- Trace elements consistent with rhyolite extraction from mush leaving behind cumulate diorite residue

Supporting Information:

- Readme
- Figures S1–S3
- Tables S1–S5

Correspondence to:

M. L. Coombs,
mcoombs@usgs.gov

Citation:

Coombs, M. L. and J. A. Vazquez (2014), Cogenetic late Pleistocene rhyolite and cumulate diorites from Augustine Volcano revealed by SIMS ^{238}U - ^{230}Th dating of zircon, and implications for silicic magma generation by extraction from mush, *Geochem. Geophys. Geosyst.*, 15, 4846–4865, doi:10.1002/2014GC005589.

Received 1 OCT 2014

Accepted 16 NOV 2014

Accepted article online 20 NOV 2014

Published online 15 DEC 2014

Cogenetic late Pleistocene rhyolite and cumulate diorites from Augustine Volcano revealed by SIMS ^{238}U - ^{230}Th dating of zircon, and implications for silicic magma generation by extraction from mush

Michelle L. Coombs¹ and Jorge A. Vazquez²

¹Alaska Volcano Observatory, U.S. Geological Survey, Anchorage, Alaska, USA, ²SHRIMP-RG Laboratory, U.S. Geological Survey, Menlo Park, California, USA

Abstract Augustine Volcano, a frequently active andesitic island stratocone, erupted a late Pleistocene rhyolite pumice fall that is temporally linked through zircon geochronology to cumulate dioritic blocks brought to the surface in Augustine's 2006 eruption. Zircon from the rhyolite yield a ^{238}U - ^{230}Th age of \sim 25 ka for their unpolished rims, and their interiors yield a bimodal age populations at \sim 26 ka and a minority at \sim 41 ka. Zircon from dioritic blocks, ripped from Augustine's shallow magmatic plumbing system and ejected during the 2006 eruption, have interiors defining a \sim 26 ka age population that is indistinguishable from that for the rhyolite; unpolished rims on the dioritic zircon are dominantly younger (\leq 12 ka) indicating subsequent crystallization. Zircon from rhyolite and diorite overlap in U, Hf, Ti, and REE concentrations although diorites also contain a second population of high-U, high temperature grains. Andesites that brought dioritic blocks to the surface in 2006 contain zircon with young (\leq 9 ka) rims and a scattering of older ages, but few zircon that crystallized during the 26 ka interval. Both the Pleistocene-age rhyolite and the 2006 dioritic inclusions plot along a whole-rock compositional trend distinct from mid-Holocene-present andesites and dacites, and the diorites, rhyolite, and two early Holocene dacites define linear unmixing trends often oblique to the main andesite array and consistent with melt (rhyolite) extraction from a mush (dacites), leaving behind a cumulate amphibole-bearing residue (diorites). Rare zircon antecrysts up to \sim 300 ka from all rock types indicate that a Quaternary center has been present longer than preserved surficial deposits.

1. Introduction

Uncertain petrologic relations between plutonic and volcanic rocks complicate understanding the differentiation pathways that yield eruptible volumes of silicic magma at arc volcanoes, as well as the batholiths that constitute the continents. End-member interpretations are that plutonic rocks exposed in dissected arcs represent magma compositions with geochemical diversity that primarily reflects melting of source rocks rather than fractionation in shallow magma chambers [e.g., Glazner *et al.*, 2008; Reubi and Blundy, 2009], or that subvolcanic plutonic rocks are the crystal-liquid residua of fractionated magmas that have been extracted and in many cases erupted [e.g., Deering and Bachmann, 2010]. Melt extraction from crystal-rich "mushy" intermediate magmas is implicated in the generation of low-temperature crystal-poor rhyolite magma in a variety of tectonic settings [e.g., Bachmann and Bergantz, 2004]. However, whether plutonic rocks contain unequivocal geochemical signatures expected for a residue from which silicic melt has been extracted remains contentious (see discussion in Deering and Bachmann [2010]), and a fractionation signature in volcanic magmas is commonly overprinted by late-stage mixing [Deering *et al.*, 2011].

Plutonic blocks entrained by ascending magmas can be direct samples of the intrusive interiors of active volcanic systems [Arculus and Wills, 1980; Bacon *et al.*, 2000, 2007; Schmitt, 2006; Vazquez *et al.*, 2007] and provide opportunities to understand plutonic-volcanic links. Although the plutonic and volcanic rocks from an individual magmatic system may form a coherent geochemical suite, confirming a petrogenetic relation requires demonstrating an association not only in space but also time. Consequently, high-resolution geochronology is critical for identifying whether volcanic-plutonic pairs are cogenetic [e.g., Tappa *et al.*, 2011].

Like many subduction zone stratovolcanoes, Augustine Volcano, Alaska erupts dominantly andesites and dacites, but is capable of producing more explosive eruptions of silicic magma as evidenced by a late Pleistocene rhyolite fall deposit on the volcano's south flank [Waitt and Begét, 2009]. To assess the chances of future large versus modest explosive eruptions at Augustine, a refined chronology and understanding of silicic magma petrogenesis are required.

Here we present evidence from U-Th zircon geochronology and whole-rock and mineral geochemistry that Augustine's late Pleistocene rhyolite, and dioritic blocks later erupted in 2006, are coeval and complementary extracted liquid and melt-depleted crystal mush, derived from dacitic bulk magma that differentiated in the upper crustal portion of the magmatic system about 25 kyr ago. The youth of the magmatic processes preserves compositions and textures little obscured by intrusive processes and demonstrate contemporaneity at a resolution that is often impossible to establish for the exhumed intrusive portions of dissected arcs.

2. Analytical Methods

Whole-rock major and trace-element concentrations were determined by GeoAnalytical Laboratories (Washington State University). Fe-Ti oxide and glass from polished thin sections were analyzed with a JEOL 8900 electron microprobe at the USGS in Menlo Park, California. Matrix glasses were analyzed using a 5 μm , 10 nA beam, and Na was analyzed first to minimize drift. Each reported analysis is the average of 11–23 spot analyses per sample. Oxides were analyzed using a 30 nA focused beam, with 30 s peak count times. Crystals are unzoned and thus we report averages of 4–5 spot analyses per crystal.

Zircon crystals were separated from \sim 0.2 to 2 kg of crushed hand samples using standard heavy liquid techniques. Crystals used for unpolished rim analyses (both unknowns and standards) were bathed in hydrofluoric acid at room temperature for 3–5 min to remove adhering glass. These zircon crystals were then pressed into indium-filled troughs within standard 25 mm diameter epoxy mounts. Crystals and standards used for interior analyses were mounted in epoxy mounts, ground to expose cross sections of crystals, polished, and imaged with petrographic and scanning electron (SEM) microscopes. Spots for SIMS analyses were selected on the basis of internal zoning revealed in cathodoluminescence (CL) images. Prior to analyses, the mounts were washed with soapy deionized water and dilute HCl solutions, and coated with 100 nm of gold.

SIMS analyses were conducted using the Stanford-USGS SHRIMP-RG ion microprobe. A primary beam of O_2^- with intensities of \sim 6 nA for U-Pb analyses and \sim 10–20 nA for ^{238}U - ^{230}Th analyses was focused into a 20–40 μm diameter elliptical area to generate positive secondary ions. The primary beam was rastered for 90–120 s over the analysis area before data collection. The mass spectrometer was tuned to a mass resolution of \sim 8000 in order to fully resolve potential isobaric interferences, and the energy selection slit set to sample secondary ions at a >40 eV offset. For U-Th analyses, secondary ion intensity was measured for $^{90}\text{Zr}_2^{16}\text{O}^+$, $^{180}\text{Hf}^{16}\text{O}^+$, $^{238}\text{U}^{16}\text{O}^+$, $^{232}\text{Th}^{12}\text{C}$ (\sim 244 amu), $^{230}\text{Th}^{16}\text{O}^+$, background at 0.05 amu above $^{230}\text{Th}^{16}\text{O}^+$, $^{232}\text{Th}^{16}\text{O}^+$, and $^{238}\text{U}^{16}\text{O}^+$ using a single axial electron multiplier. Relative ionization between U and Th was constrained by repeated intrasession measurement of the natural ^{238}U - ^{230}Th secular equilibrium value ($^{230}\text{Th}/^{238}\text{U} = 1.694 \times 10^{-5}$) in \sim 770 ka Bishop Tuff zircon. Analysis of AS3 zircon [Paces and Miller, 1993] as a secondary secular equilibrium standard corrected for relative U and Th ionization yielded a weighted mean $^{230}\text{Th}/^{238}\text{U}$ activity ratio, denoted $(^{230}\text{Th})/(^{238}\text{U})$, of 1.02 ± 0.02 . Trace and minor element concentrations in zircon were determined relative to an in-house concentration standard (MAD) [Barth and Wooden, 2010] using measured intensities normalized to measured Zr_2O^+ . Analyses of zircon standard 91500 relative to MAD yields concentrations within the ranges reported in Wiedenbeck *et al.* [2004]. Ti concentrations are calibrated to zircon standard SL-13 (6.14 ppm) [Hiess *et al.*, 2008]. U-Pb ages were determined relative to zircon standard R33 (419 Ma, quartz diorite of Braintree complex, Vermont [Black *et al.*, 2004]) and followed the analysis protocol described by Claiborne *et al.* [2006]. Raw data for both U-Pb and U-Th analyses are corrected for 25 ns deadtime, with ratios and their uncertainties derived using SQUID2 version 2.51 software and Isoplot version 3.76 [Ludwig, 2009].

U-Th isotope compositions for whole rocks were determined using a Nu high-resolution multicollector inductively coupled mass spectrometer at University of California-Davis following the sample preparation and analytical protocol described by Stelten and Cooper [2012].

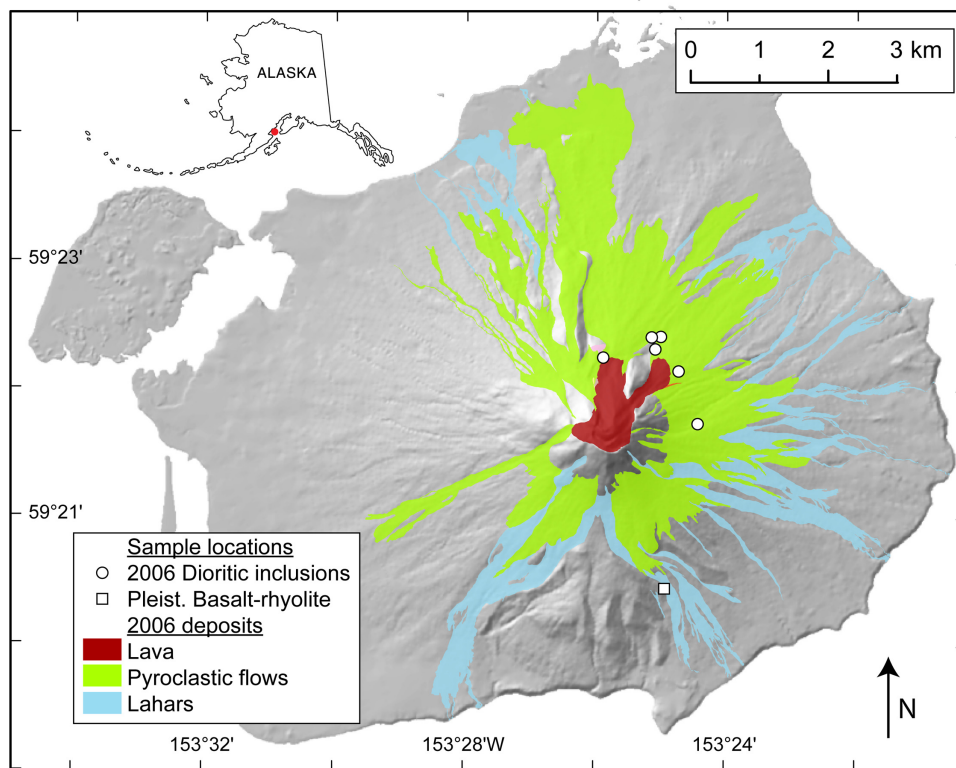


Figure 1. Shaded relief map of Augustine Island showing distribution of deposits from the 2006 eruption, and locations of samples used in this study. Inset map shows location of Augustine Island in southcentral Alaska.

3. Augustine Volcano

Augustine Volcano (Figure 1) forms an island in Alaska's Cook Inlet and is one of the most active in the Aleutian-Alaska arc. The oldest volcanic deposits preserved on the island are ~40 ka [Waitt and Begét, 2009], making this volcano's exposed edifice much younger than others in the eastern arc. Its lack of older volcanic rocks may be due to periodic scouring by Pleistocene ice sheet lobes due to its position in glacially vulnerable Cook Inlet, whereas neighboring volcanoes sit high atop mountain ranges.

The oldest exposed products from Augustine are late Pleistocene pyroclastic deposits [Johnston, 1978; Waitt and Begét, 2009] that crop out on the south flank of the volcano (Figure 1). Near the base of this section is a breccia bed of palagonitized olivine basalt to basaltic andesite bombs up to 20 cm in diameter as well as sparser radially fractured clasts of dense juvenile rhyolite. The upper 20 cm of basaltic andesite breccia is interlayered with the base of a pumiceous rhyolitic fall deposit (supporting information Figure S1). Waitt and Begét [2009] interpret this sequence as due to a submarine or subglacial basaltic andesite flank eruption and a subsequent explosive eruption of rhyolite from a summit vent. Elsewhere on the volcano's south flank, rhyolite pumice fall of the same composition sits immediately on glaciofluvial deposits [Wallace and Coombs, 2013], suggesting that the mafic portion of the eruption was quite localized and small in volume.

Deposits from early to middle Holocene Augustine eruptions are scarce and limited to a few tephra exposures on the south flank and some distal ashes with Augustine compositional affinities, whereas the late Holocene record is relatively complete and indicates that Augustine produces thick tephra falls, an apron of fragmental flowage deposits, and an edifice consisting of overlapping lava domes and short, thick flows [Waitt and Begét, 2009]. Repeated edifice failures and debris avalanches also mark the late Holocene record, with the most recent in 1883 [Begét and Kienle, 1992; Siebert et al., 1995].

Augustine erupted historically in calendar years 1883, 1935, 1964, 1976, 1986, and 2006, each time producing ashfall, pyroclastic flows, and lava domes. The 2006 eruption unfolded much like those in 1986 and 1976, with an explosive onset in January, tapering to continuous lava effusion and pyroclastic flow

production, to a short hiatus and finally effusion of a dome and two lava flows through mid-March [Coombs *et al.*, 2010].

3.1. Holocene Andesite Array

Holocene lavas and pumices including those erupted in 2006, span a compositional range of 56–64 wt. % SiO₂, with rare early Holocene tephras as evolved as 67 wt. % SiO₂ (Figure 2). Holocene andesites are calc-alkaline, low-K, and most plot as linear arrays on oxide and element variation diagrams, though there is more scatter at the SiO₂-rich end of some arrays. Disequilibrium phenocryst assemblages and textures, as well as macroscopic compositional banding, characterize the andesites and implicate magma mixing [Johnston, 1978; Larsen *et al.*, 2010; Roman *et al.*, 2005]. Quenched magmatic inclusions (QMI) in debris-avalanche blocks and pyroclasts extend the Holocene compositional range to as primitive as 51.5 wt. % SiO₂, and are interpreted as slightly mixed high-alumina, low-K basalt that is the mafic input into the Augustine system [Steiner *et al.*, 2012].

Two early Holocene tephra fall deposits, dated at $\geq\sim 6800$ ¹⁴C yr B.P. [Wallace and Coombs, 2013], have 63 and 67 wt. % SiO₂ and fall off the andesite array for many elements. They have higher Al₂O₃, P₂O₅, and Sr, and lower K₂O, Sc, and Zr at a given SiO₂ content (Figures 2 and 3).

Recently erupted andesites last staged in the shallow crust (4–6 km) as evidenced by GPS [Cervelli *et al.*, 2010] and melt-inclusion volatiles [Roman *et al.*, 2005; Webster *et al.*, 2010]. The current Augustine magmatic system is relatively oxidized ($fO_2 \approx NNO + 1.5$ log units) as evidenced by euhedral, touching magnetite-ilmenite pairs in high-silica andesite from 2006 (Figure 4 and supporting information Table S2) [Larsen *et al.*, 2010], and from late Holocene prehistoric tephras [Tappan *et al.*, 2009].

3.2. Late Pleistocene Rhyolite and Basaltic Andesite

The only identified Augustine products to fall outside the main andesite array, except for QMI, are the Pleistocene basalt to basaltic andesite (51–55 wt. % SiO₂; hereafter referred to as basaltic andesite) breccia that grades upward into the bedded rhyolitic (71–74 wt. % SiO₂) fall deposit. The rhyolite pyroclasts contain up to 10% phenocrysts of quartz, plagioclase, amphibole, and oxides in high-silica rhyolite glass (76–77 wt. % SiO₂). The rhyolites contain higher LILE, LREE, U, Th, and Pb concentrations than other Augustine magmas, but their MREE and HREE concentrations are lower and their normalized (M-H)REE patterns are concave-up (Figure 3 and Table 1) [Larsen *et al.*, 2010]. Both mafic and silicic components from this eruption fall along a lower K₂O trend than those from most Holocene Augustine eruptions (Figure 2). The basaltic andesite breccia clasts have up to 40% crystals and compositions that suggest they have accumulated clinopyroxene [Daley, 1986; Zimmer *et al.*, 2010]. The basaltic andesites are unusually volatile-rich, with ~6.5 wt. % H₂O and up to 5000 ppm S [Zimmer *et al.*, 2010].

3.3. Dioritic Inclusions From the 2006 Eruption

Within deposits of the waning stages of the 2006 eruption are salt-and-pepper, crystal-rich inclusions and blocks (“fine-grained gabbroic inclusions” of Larsen *et al.* [2010]), some as large as 6 m in diameter (supporting information Figure S1). They lack the fine-grained quenched margins or fluidal and cuspatate shapes of quenched magmatic inclusions [e.g., Bacon, 1986], instead appearing to be fragments of a fine-grained intrusion. They consist of plagioclase > amphibole \approx 2 pyroxenes >> Fe-Ti oxides >> apatite >> zircon, with up to 35 vol. % glass [Larsen *et al.*, 2010]. Plagioclase crystals are coarsely sieved and skeletal, and amphibole crystals are resorbed and rarely poikilitic with inclusions of plagioclase (supporting information Figure S2).

Whole-rock compositions for six plutonic inclusions range from 56.1 to 58.2 wt. % SiO₂ and plot offset along a distinctly lower K₂O trend relative to other 2006 and late Holocene samples (Figure 2 and Table 1). Matrix glasses are rhyolitic (78–79.1 wt. % SiO₂; Figure 2 and supporting information Table S3). While their modal crystal populations would classify the rocks as gabbro or diorite, their contents of interstitial silicic glass are such that their norms contain 10–15 wt. % quartz, and the rocks would be classified as quartz diorites if fully crystallized [Streckeisen, 1976]. The rocks will be referred to as dioritic due to this classification ambiguity. They have elevated concentrations of Sr, P, Y, MREEs, and HREEs relative to the andesite array, and lower concentrations of transition metals, LILE, HFSE, and Th, U, and Pb (Figures 2 and 3).

4. Zircon U-Th Geochronology and Trace-Element Composition

Zircon crystals from a dense rhyolite clast (NY12) from the south-flank outcrop, three dioritic inclusions (27c, 42a, and 304a) from the 2006 pyroclastic-flow deposits, and three high-silica andesite pumices (304b, 304c,

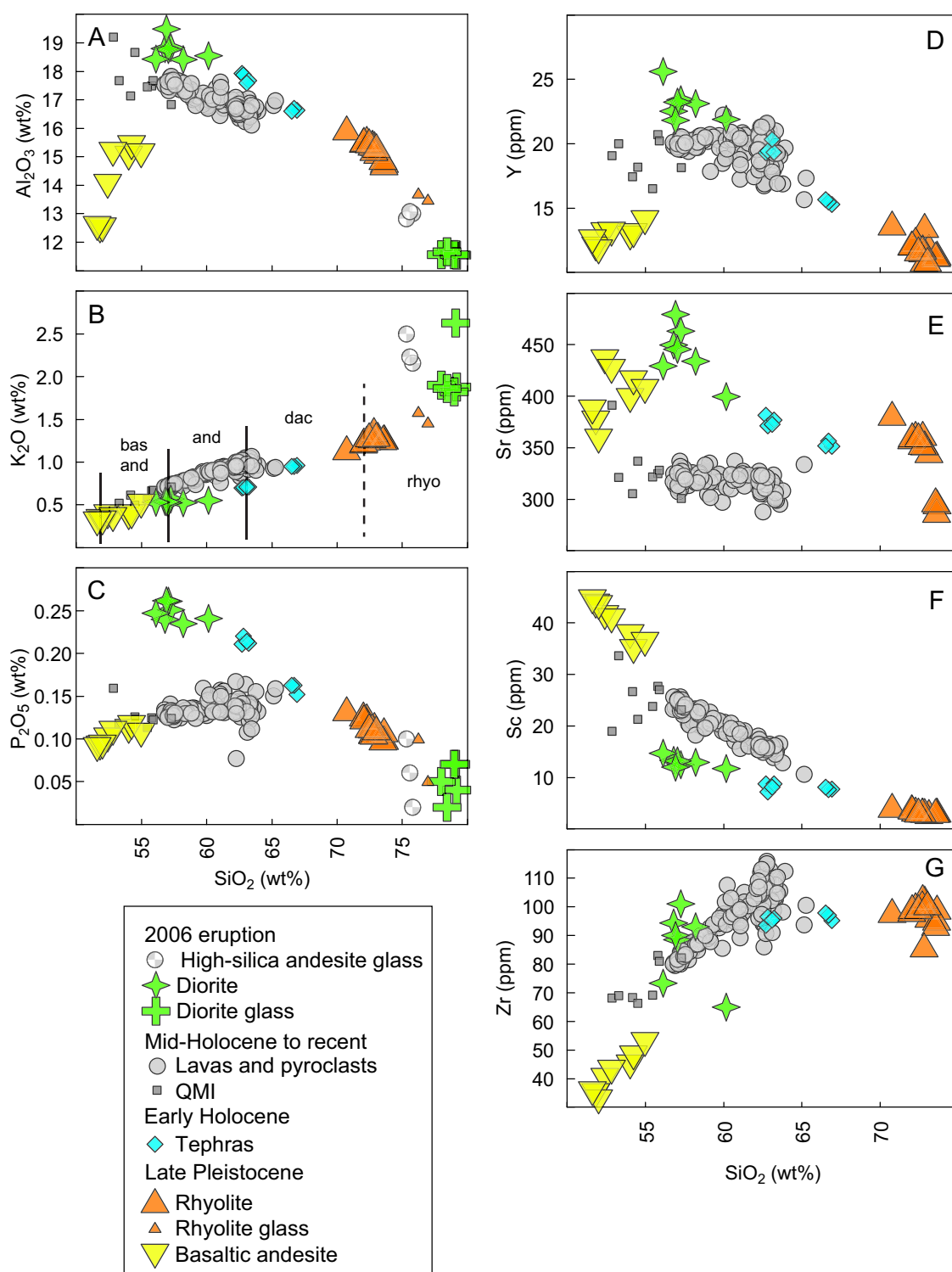


Figure 2. Compositions of eruptive products of Augustine Volcano. (a–c) Whole-rock and glass major-element variation diagrams. (d–g) Whole-rock trace-element variation diagrams. Note different x axis scale. Data from Larsen et al. [2010], Steiner et al. [2012], Wallace and Coombs [2013], and this study. QMI: quenched mafic inclusions. Lavas from 2006 are included in Mid-Holocene to recent and symbolized as gray circles.

and 310) also from the 2006 pyroclastic-flow deposits were cast in epoxy mounts, ground to expose cross sections of crystal interiors, and polished (Figures 5a and 5b). Subsets of zircon from NY12, 27c, 304b, and 310 were pressed into indium mounts to analyze their unpolished grain faces and date their final increment of crystallization (Figures 5c and 5d). Individual crystallization ages for zircon are calculated using the U-Th

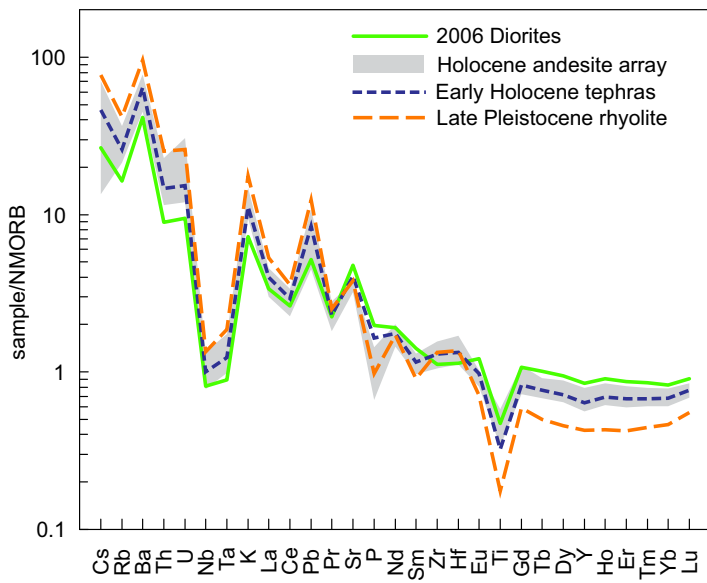


Figure 3. Averaged NMORB-normalized trace-element abundances for 2006 diorite, Pleistocene rhyolite, Holocene andesite array, and early Holocene dacites. Note the early Holocene dacite trace-element pattern typically falls between the those of the rhyolite and diorite.

method of *Sambridge and Compston* [1994] yields a majority (~60%) population with an apparent age of 26 ± 5 ka (2σ) and a minority with an age of 41 ± 9 ka (Figure 6a). The interiors of two crystals yield model ages of >200 ka, with high errors (Figure 7). Where more than one spot was analyzed on a single crystal, cores yield slightly older model ages (Figure 5a). The unpolished faces of zircon from the rhyolite yield a model age spectrum indicating a dominant (~90%) population with an apparent age of 25 ± 6 and a minority with an age of 41 ± 19 ka.

Interiors of zircon from the rhyolite have Hf concentrations mostly between 7000 and 11,000 ppm, U concentrations of ≤ 250 ppm, and Ti concentrations between 3 and 15 ppm (Figures 6–8). These Ti values yield apparent temperatures of 670–800°C using the average value of rhyolite $a\text{TiO}_2$ (0.85; obtained by touching Fe-Ti oxide pairs using activity model of *Ghiorso and Evans* [2008]) and the formulation of *Ferry and Watson* [2007] (Figure 8).

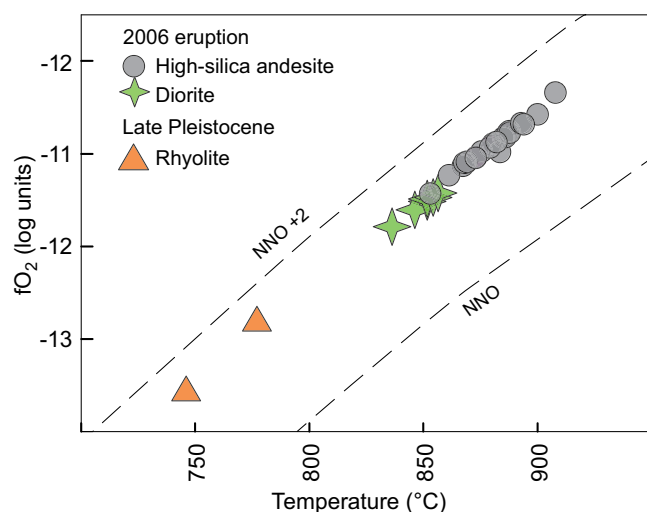


Figure 4. Temperature versus oxygen fugacity estimated from touching Fe-Ti oxide pairs using the algorithm of *Ghiorso and Evans* [2008]. Data from *Larsen et al.* [2010] and this study.

isotope composition of their host rocks (Table 2) as a model for initial $^{230}\text{Th}/^{232}\text{Th}$ during crystallization [e.g., *Reid et al.*, 1997].

Augustine zircon have low U concentrations (mostly < 300 ppm), consistent with low abundances in the whole rock (< 1.8 ppm). This yields high errors for individual U-Th model ages (Table 3).

4.1. Late Pleistocene Rhyolite

Interiors ($n = 20$ for 17 individual crystals) and unpolished rims ($n = 30$ for 30 individual crystals) for zircon from the rhyolite are in $^{238}\text{U}-^{230}\text{Th}$ disequilibrium and yield late Pleistocene model ages for crystallization. Deconvolution of ages for interiors into Gaussian populations using the mixture modeling

Chondrite-normalized REE concentrations for zircons from all Augustine samples share the same general pattern. Augustine zircons have steeply positive, slightly curved normalized REE patterns with positive Ce anomalies, similar to other igneous zircon [*Hoskin and Schaltegger*, 2003] (Figure 9). However, the Augustine zircons are unusual because they have only slightly negative to absent Eu anomalies. Rhyolite zircon REE patterns overlap with those of the diorite samples, with the exception of high-U diorite grains, discussed below.

Table 1. Representative Whole-Rock Compositions for Rhyolites, Diorites, and Andesites From Augustine Volcano^a

Sample ID	NY12	NY13	304b	304c	310	012a	013a	027a	027c	042a	304a
Eruption age	Pleist.	Pleist.	2006	2006	2006	2006	2006	2006	2006	2006	2006
Rock name	Dense rhyolite	Rhyolite pumice	Andesite	Andesite	Andesite	Diorite	Diorite	Diorite	Diorite	Diorite	Diorite
<i>Major Element (in wt %), by XRF, Normalized to 100%</i>											
SiO ₂	73.61	72.85	62.37	62.75	62.75	56.13	57.05	56.80	57.25	56.94	58.20
TiO ₂	0.20	0.22	0.56	0.55	0.55	0.63	0.60	0.61	0.58	0.57	0.57
Al ₂ O ₃	14.72	15.39	16.77	16.59	16.68	18.43	18.76	18.80	18.84	19.49	18.41
FeO(t)	1.93	1.99	5.28	5.23	5.21	8.02	7.44	7.47	7.22	6.78	7.41
MnO	0.11	0.13	0.12	0.13	0.12	0.21	0.19	0.19	0.18	0.18	0.18
MgO	0.69	0.65	3.23	3.22	3.18	3.81	3.23	3.41	3.18	3.05	2.96
CaO	3.11	3.16	6.70	6.55	6.50	8.58	8.28	8.34	8.24	8.49	7.81
Na ₂ O	4.25	4.22	3.84	3.83	3.84	3.41	3.66	3.59	3.70	3.71	3.70
K ₂ O	1.27	1.27	1.00	1.02	1.02	0.53	0.52	0.54	0.57	0.54	0.52
P ₂ O ₅	0.11	0.11	0.13	0.14	0.14	0.25	0.26	0.24	0.25	0.26	0.23
Analytical total	100.00	97.45	98.84	99.07	99.03	98.90	99.82	98.43	99.10	98.18	99.03
<i>Trace Elements (in ppm), by ICP-MS Unless Indicated</i>											
La	12.87	14.16	11.12	11.42	11.43	8.97	8.82	8.59	9.39	8.92	8.78
Ce	25.66	29.01	23.91	24.40	24.34	21.34	20.56	19.94	21.75	20.70	20.12
Pr	3.13	3.61	3.20	3.30	3.30	3.26	3.04	2.97	3.20	3.03	2.98
Nd	11.62	13.71	13.73	13.90	13.92	15.28	14.36	14.00	15.01	14.12	13.75
Sm	2.19	2.64	3.32	3.37	3.38	4.17	3.80	3.65	3.88	3.54	3.59
Eu	0.68	0.77	1.01	1.03	1.05	1.30	1.25	1.21	1.29	1.24	1.22
Gd	1.92	2.34	3.42	3.47	3.47	4.33	4.00	3.81	3.93	3.67	3.75
Tb	0.30	0.38	0.59	0.60	0.60	0.74	0.66	0.64	0.66	0.61	0.66
Dy	1.84	2.35	3.71	3.78	3.79	4.68	4.20	4.08	4.21	3.91	4.12
Ho	0.40	0.48	0.80	0.81	0.82	1.00	0.89	0.85	0.90	0.83	0.88
Er	1.15	1.41	2.29	2.32	2.28	2.83	2.53	2.43	2.53	2.39	2.49
Tm	0.19	0.22	0.35	0.36	0.35	0.43	0.38	0.37	0.38	0.36	0.38
Yb	1.31	1.55	2.28	2.33	2.32	2.72	2.46	2.40	2.51	2.34	2.46
Lu	0.23	0.27	0.38	0.38	0.38	0.45	0.41	0.40	0.42	0.39	0.40
Ba	618	619	451	464	468	264	259	267	274	275	275
Th	2.84	3.12	2.21	2.27	2.30	1.15	1.05	1.15	1.16	1.07	1.09
Nb	3.42	3.19	2.91	2.93	2.94	1.97	1.87	1.95	2.09	1.86	1.97
Y	11.3	13.5	21.3	21.5	21.6	25.6	23.2	22.5	23.4	21.8	23.1
Hf	2.68	2.92	3.16	3.18	3.18	2.20	2.45	2.55	2.68	2.43	2.50
Ta	0.27	0.24	0.23	0.22	0.21	0.13	0.12	0.12	0.13	0.12	0.12
U	1.09	1.19	0.92	0.95	0.95	0.46	0.43	0.48	0.48	0.45	0.47
Pb	3.56	3.66	2.73	2.76	2.84	1.77	1.49	1.53	1.84	1.63	1.43
Rb	24.47	23.67	19.21	19.73	19.67	9.23	8.94	9.42	10.01	9.51	9.06
Cs	0.57	0.52	0.43	0.44	0.45	0.20	0.19	0.20	0.21	0.20	0.18
Sr	287	353	319	317	321	431	447	450	463	479	434
Sc	3.31	3.17	16.18	15.99	15.66	14.71	13.26	13.31	12.49	11.99	12.86
Zr	95	102	112	116	115	73	89	94	101	90	93
Ni_xrf	5	7	20	21	21	5	5	4	4	3	6
Cr_xrf	4	5	42	43	39	2	2	2	3	2	3
V_xrf	20	12	130	126	129	155	139	150	138	129	129
Ga_xrf	17	14	18	18	16	19	19	19	20	20	20
Cu_xrf	2	5	24	27	18	21	15	19	21	11	53
Zn_xrf	43	45	57	59	58	83	75	77	75	72	73

^aWhole-rock data for samples 12a, 13a, 27a, 42a, NY12, and NY13 from Larsen et al. [2010]. Analyses for Alaska Volcano Observatory by GeoAnalytical Laboratories, Washington State University.

4.2. Dioritic Inclusions

The interiors of zircon from the dioritic samples 27c and 42a yield ^{238}U - ^{230}Th age populations of 28 ± 5 and 24 ± 5 ka, which are indistinguishable from the zircon interiors and rims from the late Pleistocene rhyolite (Figure 6b). Several dioritic zircons have interiors that are as old as ~ 260 ka (Figure 7). Dioritic sample 304a has younger zircon cores (8 ± 5 ka). Rims on zircon from dioritic sample 27c mostly yield model ages that are younger than their interiors, with an apparent age population at 11.5 ± 1.2 ka ($F = 0.67$). However, a subset of zircon rims with ^{238}U / ^{232}Th activity ratios <8 define a horizontal (zero-age) isochron (Figure 10), suggesting a somewhat higher initial $^{232}\text{Th}/^{230}\text{Th}$ for these rims than indicated by the whole-rock composition and crystallization within millennia of the 2006 eruption. A significant fraction of rims yield model ages defining a population at 29 ± 3 ka, which is indistinguishable from the rhyolite-hosted zircon. Two diorite zircon in secular equilibrium for $(^{230}\text{Th})/(^{238}\text{U})$ yielded U-Pb ages of ~ 90 Ma and 1800 Ma (Table 4).

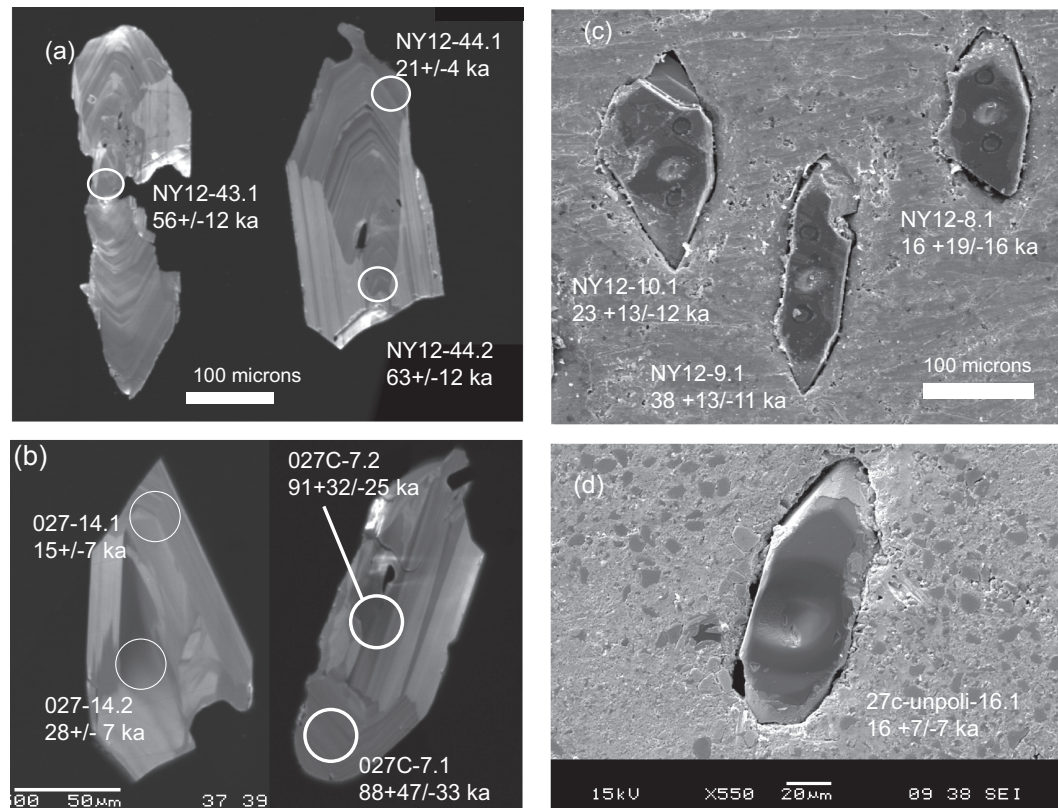


Figure 5. Zircon images. (a) CL image of polished zircon from NY12 (Mount US30). (b) SE image of unpolished, indium-mounted zircon from NY12 (Mount US31). (c) CL image of polished zircon from diorite 27c, mount US13. (d) SE image of unpolished, indium-mounted zircon from diorite sample 27c (mount US31).

U concentrations of dioritic zircon are more variable than those from rhyolite and range from near zero to 700 ppm, including a distinct cluster of ~25 ka grains that range from 400 to 700 ppm U (Figures 6b and 8). These high-U zircon have low Hf (<0.85 wt %) and high Ti (20–50 ppm). They also have elevated REE abundances relative to all other analyzed Augustine zircon (Figure 9).

Ti concentrations for high-U zircon are consistent with apparent temperatures of ~850 to greater than 950°C, using the range of αTiO_2 of 0.67–0.77 calculated using touching Fe-Ti oxide pairs from diorite samples (Figure 8). It is possible that Fe-Ti oxides record αTiO_2 that is lower than that of the melt the zircon originally crystallized in, and αTiO_2 is best reflected by rhyolite Fe-Ti oxides, which yield αTiO_2 of ~0.85. In this case Ti-in-zircon records temperatures of 830–940°C. Regardless of uncertainties in absolute temperature recorded by Ti-in-zircon [e.g., Reid *et al.*, 2011], it is clear that the high-U zircon record higher temperatures than low-U grains.

Table 2. Whole-Rock U-Series Data for Andesite, Rhyolite, and Diorite From Augustine Volcano^a

Sample	Rock Type	$(^{238}\text{U})/(^{232}\text{Th})$	$(^{230}\text{Th})/(^{232}\text{Th})$
JC11	Andesite	1.315	1.546
Dupe	Andesite	1.312	1.5
JC02	Andesite	1.313	1.509
JC03	Andesite	1.316	1.562
MC09P2	Andesite	1.325	1.615
MC10P1	Andesite	1.321	1.55
Average Andesite		1.317	1.547
NY12	Rhyolite	1.03 ± 0.01	1.29 ± 0.01
027c	Diorite	1.245 ± 0.005	1.498 ± 0.005

^aAndesite values are from Thompson [2011].

4.3. 2006 Andesites

Rare, small zircons were recovered from high-silica andesites (62.5 wt % SiO₂) erupted in 2006. Unpolished zircon rims yield a population with a mean age of 9 ± 6 ka (Figure 6c), with a handful of zircon ages that are older, but notably few to none in the age range of 25 ka observed for zircon of the rhyolite and diorite. Most andesite-hosted zircon have U (20–200 ppm), Hf (0.64–0.95 wt %), and Ti (8–15 ppm) concentrations that generally overlap with the low-U diorite zircon (Figure 8), though

Table 3. SHRIMP-RG U-Series Data for Zircons From Rhyolite, Andesite, and Dioritic Blocks From Augustine Volcano, Alaska^a

Sample Name	Sample Type	$(^{238}\text{U})/(^{232}\text{Th})$	$\pm (^{238}\text{U})/(^{232}\text{Th})$	$(^{230}\text{Th})/(^{232}\text{Th})$	$\pm (^{230}\text{Th})/(^{232}\text{Th})$	Hf ppm	U ppm	Model Age (ka)	Plus (ka)	Minus (ka)
05AUNY12-31.1	s.r.	9.09	0.10	2.95	0.32	9,267	107	25	6	5
05AUNY12-32.1	s.r.	8.49	0.10	3.71	0.31	10,244	248	43	7	7
05AUNY12-33.1	s.r.	7.73	0.07	2.80	0.34	9,987	150	28	7	7
05AUNY12-34.1	s.r.	9.59	0.08	3.61	0.40	9,762	146	34	7	7
05AUNY12-35.1	s.r.	8.00	0.06	3.22	0.26	7,390	144	35	6	6
05AUNY12-36.1	s.r.	10.75	0.17	4.64	0.82	9,439	115	46	15	13
05AUNY12-37.1	s.r.	8.59	0.08	2.97	0.29	10,050	142	27	6	5
05AUNY12-38.1	s.r.	9.38	0.09	4.62	0.63	10,409	35	55	15	13
05AUNY12-38.2	s.r.	10.71	0.10	4.24	0.86	14,808	235	40	15	13
05AUNY12-39.1	s.r.	13.40	0.18	13.08	0.63	13,378	215	335	∞	83
05AUNY12-39.2	s.r.	13.82	0.16	12.28	1.06	12,258	81	214	98	51
05AUNY12-40.1	s.r.	9.11	0.37	2.50	0.69	10,687	109	18	12	10
05AUNY12-41.1	s.r.	9.64	0.10	2.91	0.51	12,236	139	23	8	8
05AUNY12-42.1	s.r.	9.30	0.12	2.51	0.59	12,090	152	17	10	9
05AUNY12-43.1	s.r.	6.93	0.14	3.66	0.36	10,042	130	56	12	11
05AUNY12-44.1	s.r.	8.48	0.07	2.60	0.24	12,047	276	21	4	4
05AUNY12-44.2	s.r.	8.52	0.16	4.56	0.43	11,668	169	63	12	11
05AUNY12-45.1	s.r.	11.00	0.21	3.81	0.58	12,937	131	32	9	8
05AUNY12-46.1	s.r.	9.74	0.10	3.21	0.67	12,417	77	27	11	10
05AUNY12-47.1	s.r.	9.81	0.08	4.06	0.34	13,760	261	41	6	6
05AUNY12-01.1	u.r.	9.89	0.14	3.74	0.70	11,090	64	35	13	11
05AUNY12-02.1	u.r.	8.02	0.44	2.99	0.57	9,736	61	30	13	11
05AUNY12-03.1	u.r.	10.30	0.15	2.84	0.80	8,660	80	20	12	11
05AUNY12-04.1	u.r.	9.13	0.13	2.64	0.57	10,786	131	20	10	9
05AUNY12-05.1	u.r.	9.13	0.12	2.25	0.62	10,571	87	14	10	9
05AUNY12-06.1	u.r.	11.03	0.30	5.19	0.84	14,464	93	54	16	14
05AUNY12-07.1	u.r.	10.69	0.15	2.71	1.13	9,161	56	17	16	14
05AUNY12-08.1	u.r.	9.74	0.08	2.44	1.22	9,544	83	16	19	16
05AUNY12-09.1	u.r.	8.54	0.14	3.49	0.58	10,392	78	38	13	11
05AUNY12-10.1	u.r.	9.55	0.12	2.88	0.78	9,467	96	23	13	12
05AUNY12-11.1	u.r.	10.07	0.09	3.51	0.98	10,007	55	31	17	15
05AUNY12-12.1	u.r.	9.88	0.18	2.10	0.84	8,814	188	11	12	11
05AUNY12-12.2	u.r.	8.81	0.10	2.64	0.48	12,766	156	21	8	8
05AUNY12-13.1	u.r.	8.50	0.07	2.91	0.58	9,699	90	27	11	10
05AUNY12-14.1	u.r.	8.65	0.15	2.86	0.58	9,589	70	25	11	10
05AUNY12-15.1	u.r.	10.17	0.08	2.61	0.75	10,095	51	17	11	10
05AUNY12-16.1	u.r.	10.14	0.20	1.51	1.44	10,235	98	3	19	16
05AUNY12-17.1	u.r.	9.54	0.10	2.90	0.67	7,924	105	23	11	10
05AUNY12-18.1	u.r.	11.40	0.10	6.21	1.30	10,948	61	70	30	23
05AUNY12-19.1	u.r.	9.81	0.08	3.32	0.46	12,161	47	29	8	7
05AUNY12-20.1	u.r.	9.21	0.16	1.95	0.68	9,325	71	9	10	9
05AUNY12-21.1	u.r.	9.52	0.09	3.09	0.84	8,984	79	26	15	13
05AUNY12-22.1	u.r.	9.69	0.31	4.36	0.45	7,213	119	48	10	9
05AUNY12-23.1	u.r.	9.56	0.26	3.90	1.06	9,461	71	40	22	18
05AUNY12-24.1	u.r.	9.56	0.12	3.66	0.82	10,149	71	36	16	14
05AUNY12-25.1	u.r.	8.81	0.31	2.67	0.82	9,628	68	21	15	13
05AUNY12-26.1	u.r.	11.62	0.10	3.20	1.02	10,294	58	22	14	12
05AUNY12-27.1	u.r.	9.70	0.34	3.73	0.82	9,573	49	36	15	14
05AUNY12-28.1	u.r.	11.72	0.19	4.42	1.18	12,099	111	38	19	16
05AUNY12-29.1	u.r.	10.57	0.14	6.28	1.61	9,015	56	81	48	33
05AUNY12-30.1	u.r.	7.51	0.11	3.49	0.34	7,862	148	45	9	8
MLC042A-1.1	s.d.	4.37	0.03	1.97	0.19	7,589	258	18	8	7
MLC042A-1.2	s.d.	5.07	0.15	2.52	0.29	7,922	193	34	12	11
MLC042A-2.1	s.d.	2.51	0.06	1.75	0.08	7,371	527	24	9	9
MLC042A-3.1	s.d.	3.15	0.06	1.89	0.09	7,434	590	25	6	6
MLC042A-3.2	s.d.	3.71	0.08	2.10	0.21	7,533	436	30	13	11
MLC042A-4.1	s.d.	4.87	0.06	2.11	0.14	7,246	443	20	5	5
MLC042A-5.1	s.d.	9.90	0.09	3.29	0.94	9,241	83	25	16	14
MLC042A-6.1	s.d.	4.90	0.06	2.36	0.14	8,043	481	29	6	5
MLC042A-6.2	s.d.	4.96	0.06	2.12	0.13	8,099	496	20	5	5
MLC042A-7.2	s.d.	4.49	0.12	5.27	0.69	10,396	70	∞	∞	∞
MLC042A-8.1	s.d.	6.36	0.12	6.50	0.59	8,888	124	413	∞	199
027C-1.1	s.d.	3.49	0.09	2.85	0.27	8,423	211	101	41	30
027C-1.2	s.d.	6.08	0.15	5.08	1.37	7,843	90	147	∞	80
027C-1.3	s.d.	7.57	0.20	2.79	0.61	7,381	223	25	14	12
027C-2.1	s.d.	4.97	0.12	2.50	0.17	7,767	522	34	7	7
027C-2.2	s.d.	2.85	0.07	1.96	0.13	8,065	410	37	13	12
027C-3.1	s.d.	4.65	0.12	2.00	0.13	7,316	615	17	5	5

Table 3. (continued)

Sample Name	Sample Type	$(^{238}\text{U})/(^{232}\text{Th})$	$\pm(^{238}\text{U})/(^{232}\text{Th})$	$(^{230}\text{Th})/(^{232}\text{Th})$	$\pm(^{230}\text{Th})/(^{232}\text{Th})$	Hf ppm	U ppm	Model Age (ka)	Plus (ka)	Minus (ka)
027C-3.2	s.d.	2.59	0.06	1.79	0.10	7,955	548	26	11	10
027C-3.3	s.d.	2.56	0.06	1.62	0.19	7,644	410	11	18	16
027C-3.4	s.d.	6.05	0.15	2.82	0.20	8,149	508	35	7	6
027C-3.5	s.d.	5.58	0.14	2.45	0.18	7,844	534	27	6	6
027C-3.6	s.d.	2.53	0.06	1.83	0.10	8,191	474	33	12	11
027C-4.1	s.d.	8.02	0.22	7.62	2.42	8,726	79	255	∞	169
027C-5.1	s.d.	8.48	0.21	4.82	0.39	11,031	345	67	12	11
027C-5.2	s.d.	9.01	0.25	6.63	0.68	10,661	214	118	34	26
027C-5.3	s.d.	8.38	0.24	5.73	0.84	9,694	142	98	38	28
027C-5.4	s.d.	10.56	0.29	11.59	1.12	10,852	147	∞	∞	∞
027C-6.1	s.d.	6.86	0.17	3.02	0.76	8,795	225	35	23	19
027C-6.2	s.d.	6.77	0.17	2.75	0.45	8,980	247	28	12	11
027C-6.3	s.d.	10.93	0.27	6.40	1.60	8,430	108	77	45	32
027C-6.4	s.d.	10.53	0.27	4.87	1.88	8,627	125	49	42	30
027C-7.1	s.d.	4.80	0.12	2.14	0.28	7,503	515	22	11	10
027C-7.2	s.d.	4.25	0.10	2.17	0.13	7,723	624	28	6	6
027C-8.1	s.d.	2.91	0.07	1.78	0.31	6,783	199	21	28	22
027C-8.2	s.d.	2.86	0.07	1.86	0.20	7,591	227	28	19	16
027C-8.3	s.d.	8.88	0.22	8.45	1.72	9,077	72	264	∞	138
027C-9.1	s.d.	12.95	0.32	10.19	1.77	9,774	106	148	98	51
027C-9.2	s.d.	7.09	0.21	3.60	0.69	8,318	149	49	22	19
027C-9.3	s.d.	7.02	0.26	7.48	2.58	9,874	65	∞	∞	∞
US013-027C-4.1	s.d.	2.67	0.02	2.06	0.15	8,241	344	55	21	18
US013-027C-4.2	s.d.	2.68	0.01	1.71	0.23	8,407	342	17	22	18
US013-027C-6.1	s.d.	2.55	0.01	1.95	0.24	8,032	347	46	36	27
US013-027C-7.1	s.d.	9.80	0.06	6.22	1.35	11,012	122	88	47	33
US013-027C-7.2	s.d.	5.54	0.06	3.93	0.48	8,120	185	91	32	25
US013-027C-8.1	s.d.	9.31	0.06	7.00	1.02	7,434	115	51	5	5
US013-027C-8.2	s.d.	12.92	0.07	11.21	1.42	11,666	169	195	140	59
US013-027C-9.1	s.d.	21.12	0.12	21.18	1.67	11,164	294	510	∞	251
US013-027C-9.2	s.d.	8.08	0.11	2.91	4.99	9,887	71	25	274	71
US013-027C-11.1	s.d.	2.30	0.01	1.65	0.08	5,281	564	17	10	9
US013-027C-12.1	s.d.	9.29	0.09	9.61	1.08	9,779	147	∞	∞	∞
US013-027C-13.1	s.d.	13.42	0.34	12.27	1.77	12,214	123	236	∞	90
US013-027C-13.2	s.d.	9.48	0.08	4.51	1.48	9,228	90	50	36	27
US013-027C-14.1	s.d.	3.96	0.02	1.84	0.16	8,087	444	15	7	7
US013-027C-14.2	s.d.	3.92	0.02	2.10	0.13	8,984	674	28	7	7
US013-027C-15.1	s.d.	5.47	0.03	2.76	0.33	4,157	149	39	13	11
10AUMC-304A-10.1	s.d.	3.65	0.04	1.64	0.07	9,203	775	3	3	3
10AUMC-304A-11.1	s.d.	2.88	0.02	1.58	0.10	9,878	305	0	7	7
10AUMC-304A-12.1	s.d.	2.26	0.02	1.60	0.09	9,813	297	4	12	11
10AUMC-304A-14.1	s.d.	2.31	0.03	1.57	0.05	8,707	780	0	6	6
10AUMC-304A-6.1	s.d.	6.75	0.22	2.29	0.35	9,200	119	16	8	8
10AUMC-304A-7.1	s.d.	5.59	0.19	3.88	0.49	11,271	175	85	33	25
10AUMC-304A-8.1	s.d.	5.69	0.10	2.07	0.27	8,406	131	13	8	7
10AUMC-304A-9.1	s.d.	5.48	0.07	1.64	0.23	9,710	173	2	6	6
027-UNPOLI-01.1	u.d.	11.13	0.15	3.91	0.63	3,740	36	31	10	9
027-UNPOLI-02.1	u.d.	6.02	0.23	1.78	0.22	5,726	132	7	5	5
027-UNPOLI-03.1	u.d.	7.78	0.11	1.74	0.33	3,135	40	4	6	6
027-UNPOLI-04.1	u.d.	4.67	0.10	1.76	0.14	2,906	131	9	5	5
027-UNPOLI-05.1	u.d.	6.59	0.09	2.12	0.22	5,216	108	13	5	5
027-UNPOLI-07.1	u.d.	2.96	0.04	1.67	0.05	4,519	482	11	4	4
027-UNPOLI-08.1	u.d.	9.19	0.72	2.96	0.52	9,502	93	22	9	9
027-UNPOLI-09.1	u.d.	11.12	0.19	2.81	0.59	8,145	61	16	8	7
027-UNPOLI-10.1	u.d.	9.12	0.21	2.82	0.66	6,231	42	20	12	11
027-UNPOLI-11.1	u.d.	8.15	0.58	2.23	0.38	5,225	58	12	7	7
027-UNPOLI-12.1	u.d.	11.24	0.18	3.40	0.61	6,762	49	23	8	8
027-UNPOLI-13.1	u.d.	9.93	0.27	3.32	0.50	7,225	77	26	8	8
027-UNPOLI-14.1	u.d.	10.41	0.26	1.95	0.52	7,764	60	5	7	6
027-UNPOLI-15.1	u.d.	9.85	0.16	5.15	0.42	7,988	122	60	10	9
027-UNPOLI-16.1	u.d.	10.12	0.16	2.71	0.49	8,377	66	16	7	7
027-UNPOLI-17.1	u.d.	8.91	0.28	2.49	0.46	8,000	76	15	8	7
027-UNPOLI-18.1	u.d.	9.17	0.17	2.35	0.42	9,491	98	12	7	6
027-UNPOLI-19.1	u.d.	11.17	0.45	2.65	0.56	7,012	53	13	7	7
027-UNPOLI-20.1	u.d.	11.03	0.36	3.00	0.74	7,893	44	18	10	9
027-UNPOLI-22.1	u.d.	11.90	0.23	4.27	0.41	8,796	120	33	6	6
027-UNPOLI-24.1	u.d.	10.91	0.49	3.66	1.02	6,634	36	28	16	14
027-UNPOLI-25.1	u.d.	11.76	0.19	4.21	0.47	9,484	110	33	7	6

Table 3. (continued)

Sample Name	Sample Type	$(^{238}\text{U})/(^{232}\text{Th})$	$\pm(^{238}\text{U})/(^{232}\text{Th})$	$(^{230}\text{Th})/(^{232}\text{Th})$	$\pm(^{230}\text{Th})/(^{232}\text{Th})$	Hf ppm	U ppm	Model Age (ka)	Plus (ka)	Minus (ka)
027-UNPOLI-26.1	u.d.	8.13	0.12	3.00	0.37	7,669	84	27	8	7
027-UNPOLI-27.1	u.d.	9.93	0.39	2.63	0.47	7,673	73	15	7	7
027-UNPOLI-28.1	u.d.	10.17	0.15	2.77	0.73	5,403	47	17	11	10
027-UNPOLI-29.1	u.d.	11.54	0.13	2.67	0.82	8,323	60	13	10	9
027-UNPOLI-31.1	u.d.	10.42	0.12	2.83	0.44	7,420	70	17	6	6
027-UNPOLI-31.1-X	u.d.	9.08	0.12	3.28	0.60	8,563	56	28	11	10
027-UNPOLI-32.1	u.d.	2.06	0.02	1.71	0.05	4,531	532	32	9	9
027-UNPOLI-32.1-X	u.d.	9.71	0.12	2.69	0.53	5,654	56	17	8	8
027-UNPOLI-33.1	u.d.	15.14	0.26	6.39	3.48	3,370	5	47	53	36
027-UNPOLI-33.1-X	u.d.	5.57	0.19	2.06	0.30	6,447	115	15	9	8
027-UNPOLI-34.1	u.d.	9.63	0.29	4.88	0.20	3,426	588	56	5	5
027-UNPOLI-34.1-X	u.d.	11.85	0.20	3.27	0.76	7,740	60	20	10	9
027-UNPOLI-35.1	u.d.	3.30	0.04	1.76	0.08	5,794	477	15	5	5
027-UNPOLI-35.1-X	u.d.	11.91	0.18	3.12	1.12	5,002	27	18	14	13
027-UNPOLI-36.1	u.d.	2.55	0.03	1.52	0.07	3,950	239	2	6	6
027-UNPOLI-36.1-X	u.d.	9.47	0.14	1.44	1.41	7,304	22	-1	20	17
027-UNPOLI-37.1	u.d.	10.43	0.12	2.56	1.85	5,839	28	13	28	22
027-UNPOLI-37.1-X	u.d.	4.13	0.05	1.67	0.11	3,365	222	7	4	4
027-UNPOLI-38.1	u.d.	16.15	0.23	8.74	0.50	10,138	249	73	8	7
027-UNPOLI-38.1-X	u.d.	9.06	0.20	4.62	0.56	6,130	59	56	14	12
027-UNPOLI-39.1	u.d.	9.54	0.19	3.38	0.66	3,487	49	28	12	11
027-UNPOLI-40.1	u.d.	10.81	0.13	2.94	0.39	5,389	65	18	5	5
027-UNPOLI-41.1	u.d.	9.43	0.16	2.11	0.49	6,683	58	8	7	7
027-UNPOLI-42.1	u.d.	12.66	0.20	3.56	0.46	4,024	66	22	6	5
027-UNPOLI-43.1	u.d.	10.61	0.15	2.67	0.74	7,193	37	15	10	9
027-UNPOLI-44.1	u.d.	9.21	0.17	2.84	0.48	3,044	35	20	8	8
027-UNPOLI-46.1	u.d.	9.42	0.14	3.95	0.76	4,116	30	39	16	14
027-UNPOLI-47.1	u.d.	6.74	0.12	2.09	0.24	5,363	105	13	5	5
027-UNPOLI-48.1	u.d.	3.27	0.05	1.80	0.10	4,596	266	18	6	6
027-UNPOLI-49.1	u.d.	9.57	0.11	4.26	0.41	4,351	66	44	8	8
027C-POL-1.1	u.d.	9.66	0.13	1.70	0.49	9,959	89	3	7	6
027C-POL-10.1	u.d.	3.78	0.07	1.73	0.10	5,747	271	10	5	5
027C-POL-11.1	u.d.	8.52	0.11	3.45	0.27	10,008	205	34	6	5
027C-POL-12.1	u.d.	8.97	0.11	3.07	0.34	8,742	124	25	6	6
027C-POL-2.1	u.d.	8.58	0.11	2.12	0.39	8,154	99	10	6	6
027C-POL-4.1	u.d.	6.79	0.15	1.26	0.37	7,736	56	-5	7	7
027C-POL-5.1	u.d.	5.20	0.11	1.88	0.10	5,772	410	11	3	3
027C-POL-6.1	u.d.	8.65	0.10	3.30	0.25	10,436	252	30	5	5
027C-POL-7.1	u.d.	2.26	0.03	1.70	0.06	6,460	430	25	9	8
027C-POL-8.1	u.d.	9.26	0.19	3.74	0.46	8,313	88	36	9	8
027C-POL-9.1	u.d.	5.98	0.08	1.66	0.34	7,060	74	4	8	8
10aumlc304b-1.1	u.a.	8.44	0.14	1.88	0.32	13,069	167	5	5	5
10aumlc304b-2.1	u.a.	10.26	0.22	5.28	0.63	13,016	125	59	14	13
10aumlc304c-1.1	u.a.	11.97	0.26	3.84	1.39	6,083	26	26	20	17
10aumlc304c-3.1	u.a.	2.17	0.05	2.31	0.09	13,521	342	222	379	74
10AUMLC310-1.1	u.a.	6.07	0.10	2.42	0.34	6,617	99	21	10	9
10aumlc310-11.1	u.a.	9.71	0.20	2.84	0.56	12,974	122	18	9	8
10aumlc310-14.1	u.a.	9.35	0.22	1.98	0.53	13,464	120	6	8	7
10aumlc310-16.1	u.a.	10.59	0.18	2.86	1.58	13,994	104	16	24	20
10aumlc310-18.1	u.a.	8.85	0.24	1.65	0.44	13,269	161	1	7	6
10AUMLC310-19.1	u.a.	7.36	0.19	9.57	3.20	8,239	70	∞	∞	∞
10AUMLC310-2.1	u.a.	7.12	0.25	3.42	0.87	7,215	57	42	27	22
10aumlc310-6.1	u.a.	8.82	0.13	3.29	0.85	9,646	58	28	17	15
10aumlc310-7.1	u.a.	8.20	0.13	2.15	0.42	13,806	165	10	8	7
10aumlc310-9.1	u.a.	5.83	0.22	2.32	0.42	10,543	119	20	13	12

^as.r. = sectioned rhyolite. u.p. = unpolished rhyolite. s.d. = sectioned diorite. p.d. = polished diorite. s.a. = sectioned andesite. Errors are 1σ . Secular equilibrium = ∞ . Activity ratios and ages calculated using decay constants: $\lambda^{238}\text{U}$ 1.55125E-10, $\lambda^{232}\text{Th}$ 4.94752E-11 [Steiger and Jäger, 1977]; $\lambda^{230}\text{Th}$ = 9.1577E-6 [Cheng et al., 2000].

two grains have higher U (Figure 7). Two rims (304c-2.1 and 3.1) have \sim 1700 ppm U (not shown), are in ^{230}Th - ^{238}U secular equilibrium, and are likely true xenocrysts.

5. Discussion

5.1. Age of the Rhyolite and Longevity of the Augustine Magmatic System

The \sim 26 ka age for both rims and majority of interiors of zircon from the rhyolite suggest a geologically brief episode of zircon crystallization. Radiocarbon dating of Augustine tephras brackets the eruption age of

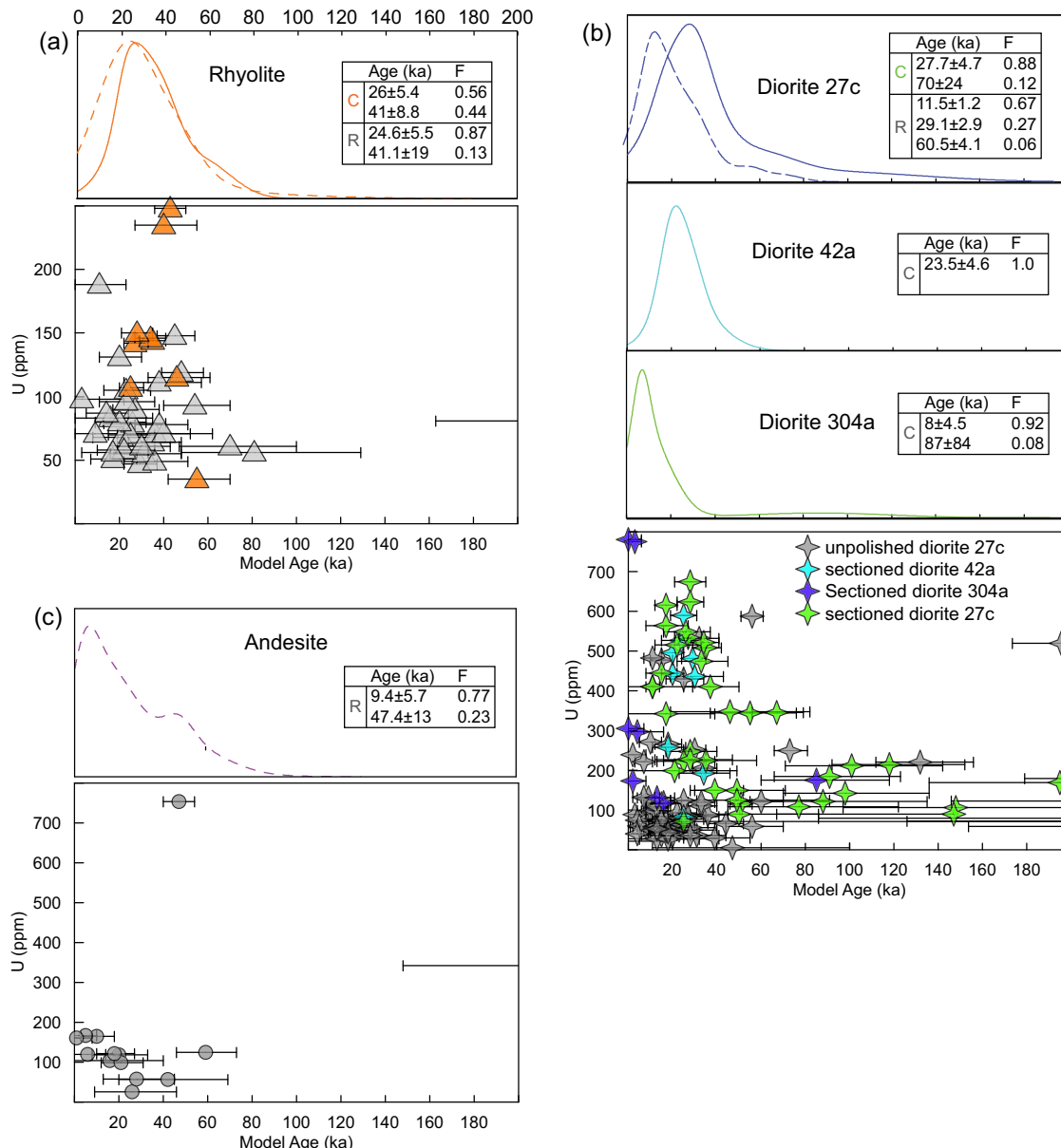


Figure 6. U-Th ages and U concentrations for zircon cores and rims from Augustine rhyolite and 2006 diorites and andesites. Probability density function curves for model ages of Augustine zircon cores (solid lines) and unpolished rims (dashed lines) based on two-point isochron slopes derived from whole-rock-zircon ($^{230}\text{Th}/^{232}\text{Th}$) and ($^{238}\text{U}/^{232}\text{Th}$) values. Insets show Gaussian age populations and 2-sigma errors determined using the *Sambridge and Compston* [1994] unmixing method in Isoplot [Ludwig, 2003]. F—population fraction. Error bars on scatterplots show 1-sigma age errors. Note some crystals yielded older model ages than are shown and can be seen in Figure 7.

the rhyolite between 8 and ~40 ka [Waitt and Begét, 2009; Wallace and Coombs, 2013]. Accordingly, eruption of the rhyolite must have occurred between ~26 and 8 ka. At one stratigraphic section on the volcano's south flank, pumiceous rhyolitic fall deposits of the same composition as the rhyolite in the rhyolite-basaltic andesite deposit overlie and are interbedded with the top of glacial and glaciofluvial deposits [Waitt and Begét, 2009], consistent with rhyolite eruption during the latest Pleistocene or earliest Holocene.

The few mid-Pleistocene zircon antecrysts from all rock types establish that a Quaternary magmatic center existed at Augustine since at least ~300 ka (Figure 7), despite the fact that the late Pleistocene rhyolite described here is near the base of the oldest stratigraphic sections on Augustine. Neighboring mainland Cook Inlet volcanoes expose lavas as old as 0.9 Ma (e.g., Redoubt [Till et al., 1994] and Spurr [Nye and Turner, 1990]). Augustine's lack of older exposed volcanic rocks may be due to periodic scouring by Pleistocene ice

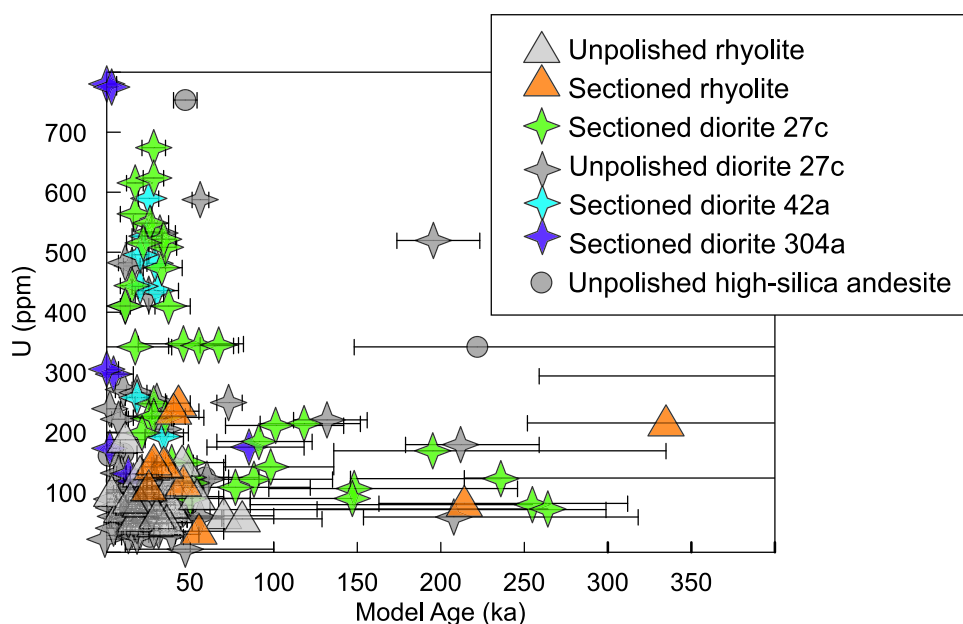


Figure 7. Zircon model ages (in ka) versus U concentration (in ppm) for all analyzed Augustine zircon, showing small numbers of crystals from all rock types older than 200 ka. Model ages calculated as in Figure 6.

sheet lobes due to its position in glacially vulnerable Cook Inlet, whereas neighboring volcanoes sit high atop mountain ranges.

The relative scarcity of zircon older than ~ 70 ka suggests that small but frequent andesitic eruptions of the sort that occurred prior to and after the generation of the Pleistocene rhyolite do not allow for significant zircon crystallization.

Finally, this study yielded only a very few truly xenocrystic zircon with ages greater than a few hundred thousand years. A single zircon dated at 1800 Ma matches in age a large population of zircon xenocrysts from Redoubt Volcano, 130 km to the north, that are thought to be sourced from igneous rocks in or below Peninsular terrane basement [Bacon *et al.*, 2011]. The presence of a similarly aged zircon under Augustine suggests the same terrane extends below lower Cook Inlet, as well.

5.2. Plutonic-Volcanic Link Between Pleistocene Rhyolite and Dioritic Inclusions

5.2.1. Geochronological Evidence

Zircon geochronology reveals that both the rhyolite and some dioritic inclusions from the 2006 eruption crystallized most of their zircon at approximately 26 ka. That rim ages of rhyolite zircon also give this age suggests that the rhyolitic magma erupted soon after, whereas younger rim ages for dioritic zircons show that overgrowth events continued into the Holocene. Concordant ages between the rhyolite and dioritic zircon establish their contemporaneity and suggest that the rocks are cogenetic.

In contrast to the complementary relation between the rhyolite and diorites, the mismatch in zircon age spectra, and offset in whole-rock chemical trends suggests that diorites are unrelated to the andesites that brought them to the surface in 2006. Dioritic inclusions erupted in 2006 average about 80 vol. % crystals, which are pervasively resorbed. Rounded Fe-Ti oxides in the diorites yield temperatures of $\sim 850^\circ\text{C}$, about 30° cooler than the andesites, but about 100°C hotter than the late Pleistocene rhyolite (Figures 4 and 11). It is likely that the dioritic intrusion was solid or nearly solid and underwent reheating upon being intruded and entrained by the 2006 andesite magmas. The scattering of Holocene rim ages for dioritic zircons may result from multiple reheating and cooling events after emplacement at 26 ka.

5.2.2. Evidence From Whole-Rock Geochemistry

In all whole-rock variation diagrams, Pleistocene rhyolite and 2006 dioritic inclusions plot along arrays that are generally linear, distinct from, and commonly oblique to, those formed by the majority of Augustine

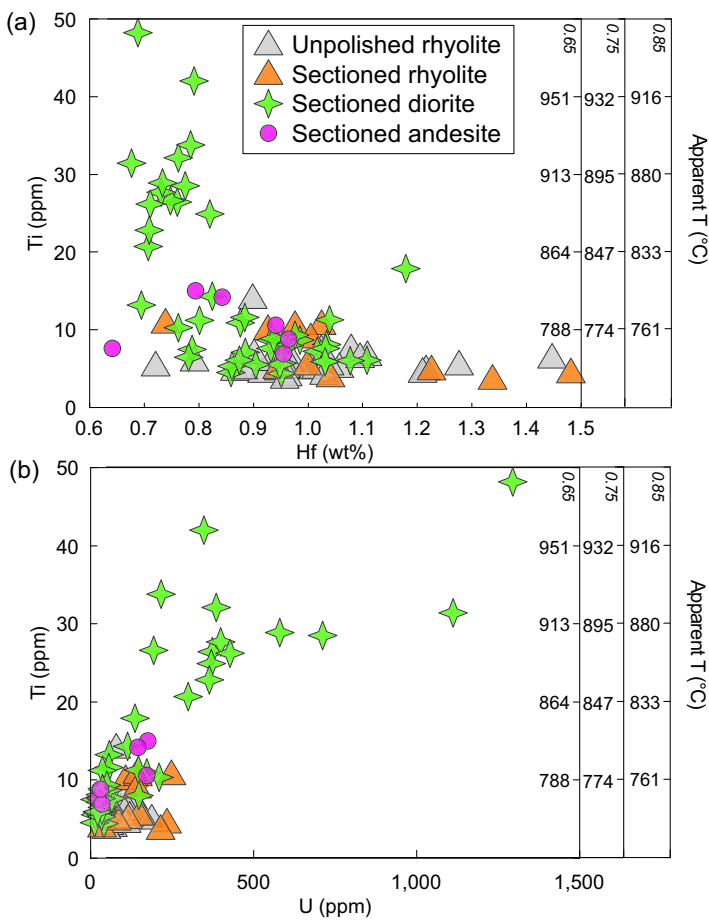


Figure 8. Results of Ti-in-zircon thermometry for Augustine zircon. (a) Hf, in wt %, and (b) U, in ppm, versus Ti, in ppm. Apparent temperatures for a range of $a\text{TiO}_2$ as calculated for Augustine samples using Fe-Ti oxide pairs are shown on the right axes. Temperature determined using Ferry and Watson [2007].

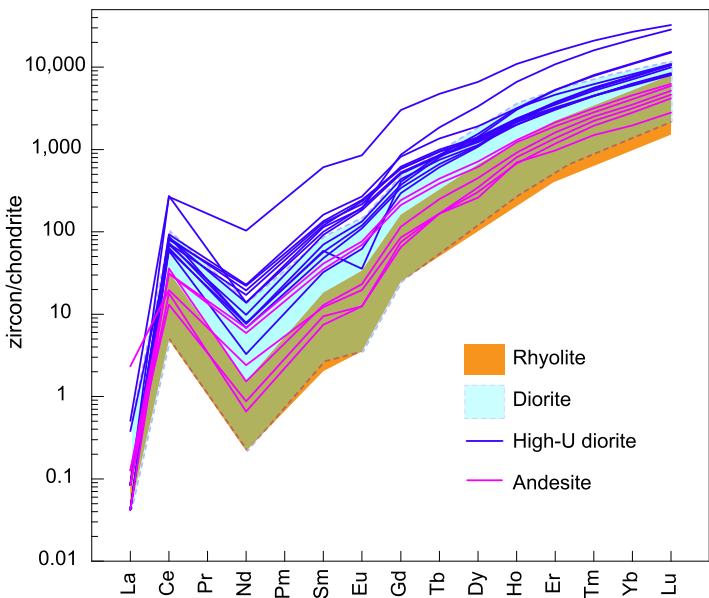


Figure 9. Chondrite-normalized REE abundances for zircon from Augustine Pleistocene rhyolite (in yellow), 2006 diorites (in blue), and 2006 high-silica andesite (black lines).

eruptive products (Figure 2). These trends are consistent with the diorites being crystal residues complementary to the rhyolite [Deering and Bachmann, 2010; Gelman et al., 2014]. Enrichments in P_2O_5 and Sr in diorite are consistent with the accumulation of apatite and plagioclase, respectively.

The rhyolite has enriched LREE, and an overall concave-up REE pattern, suggesting it separated from an amphibole-bearing residue [Davidson et al., 2013], or a “cold, wet granodiorite mush” [Bachmann and Bergantz, 2008] (Figure 3). The high $f\text{O}_2$ of the magmatic system (Figure 4) is likely responsible for the lack of significant Eu anomalies in both whole-rock and zircon REE patterns.

To evaluate if melt extraction generated the rhyolite, we can examine crystal-melt element distribution and equilibrium between the diorite residue and crystal-poor rhyolite. Assuming that the mean rhyolite represents the composition of the extracted liquid, the fraction of trapped liquid in the dioritic cumulates can be estimated assuming an appropriately low D for some highly incompatible trace element. Assuming $D_{\text{Cs}} = 0.001$ gives trapped liquid fractions of 0.33–0.37. Numerically removing these trapped liquid fractions and normalizing to the mean rhyolite gives estimates of bulk Ds (Table 5). The resulting Ds are closely similar between dioritic samples (Figure 12). Sr is moderately compatible (D_{Sr} : 1.5–1.7), the REE pass smoothly with increasing atomic number from weakly incompatible (D_{La} :

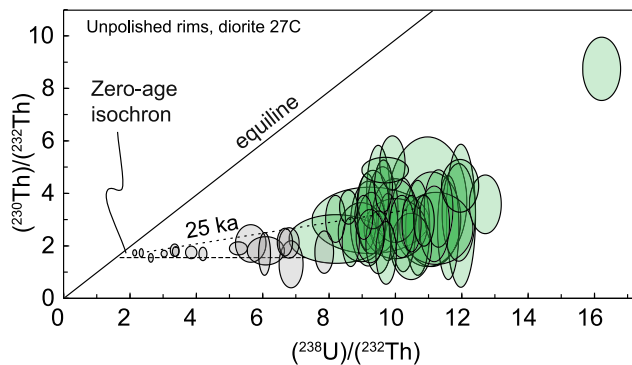


Figure 10. Activity ratio diagram for unpolished zircon rims from Augustine diorite block (sample 27c). Spot analyses fall near a zero-age isochron (gray symbols) or along a ~25 ka isochron (green symbols).

in the crystallizing assemblage, and the overall level of REE compatibility is accomplished through the presence of ~0.5 % apatite (Table 6).

For many elements and oxides, the diorite-rhyolite array crosses the evolved dacitic end of the predominantly andesitic Augustine volcanic suite (Figure 2). Such relations suggest that the bulk magma that intruded and differentiated to form the rhyolite and residual diorites was dacitic. Two early Holocene Augustine dacite (to high-silica andesite) tephras plot along the diorite-rhyolite array, even where this trend is at steep angles to the main Augustine compositional suite. We posit that these relatively silicic early Holocene tephras are magmatic equivalents to the crystal-rich intermediates from which the rhyolite was extracted (Figure 13). If so, the diorite, dacites, and rhyolite define an unmixing trend indicating that melt extraction resulted in subequal volumes of diorite and rhyolite. Because it is unknown what percent of liquid trapped in the diorite blocks was left there during this extraction, versus formed later during remelting events, it is impossible to know the crystallinity of the mush with certainty, but it appears to have been approximately 50%. Subequal amounts of melt and residue are consistent with physical models that predict melt extraction may be facilitated when a rigid framework forms at around 40–60% crystallinity [Dufek and Bachmann, 2010].

The eruption of rhyolite was coeval with eruption of basalt to basaltic andesite, the most mafic known deposits from Augustine Volcano. The basaltic andesite was exceptionally volatile rich, with undegassed olivine-hosted melt inclusions containing ~6.5 wt % H₂O and ~5000 ppm S [Zimmer et al., 2010]. An influx of volatile-rich mafic magma may have triggered melt extraction from crystal-rich magma [cf., Sisson and Bacon, 1999], and the propagation of the low-viscosity mafic dike to the surface may have provided a pathway for rhyolite to erupt.

5.2.3. Timing of Melt Extraction Versus Rhyolite Eruption

By looking at the crystals and crystal compositions in the rhyolite it is possible to determine the efficiency of melt extraction. Zircon from the diorite overlap with low-Hf zircon from the rhyolite, but the rhyolite contains a population with higher Hf (>1.2 wt %) (Figure 8). It is plausible that these zircons crystallized from the rhyolite melt after extraction, whereas the lower Hf zircon formed within the crystal-rich intermediate prior to mush extraction. That the rhyolite brought some mush zircon crystals with it is consistent with the

0.5, D_{Ce}: 0.6–0.7) to compatible, peaking from Tb (D_{Tb}: 2.3–3.0) to Er (D_{Er}: 2.4–3.0), then declining slightly to Lu (D_{Lu}: 1.9–2.3). Notably, the calculated bulk partition coefficient patterns lack Eu anomalies. Similar REE bulk partition coefficient patterns are calculated from melt-free diorite modes and literature mineral-melt partition coefficients (Table 6), indicating that the mineral assemblage of the diorites can represent a crystal-rich residue in equilibrium with the 26 ka rhyolite. The overall pattern reflects the presence of ~10% amphibole

Table 4. SHRIMP-RG U-Pb Data for Zircon From Dioritic Blocks From Augustine Volcano, Alaska^a

Sample	Spot Name	232Th/ 238U	204Pb/ 206Pb	1 sigma err %	207Pb/ 206Pb	1 sigma err %	% ²⁰⁶ Pb common	206Pb/ 238U	1 sigma % err	207-corr 206Pb/ 238U Age	1 sigma err	204corr 207Pb/ 206Pb Age	1 sigma err	U ppm	Th ppm
013a	MLC013A-1.2	0.25	3.40E-04	42	0.113	0.7	1.12	0.279	0.4	1561.4	6.6	1778	36	297	71
027c	MLC027C-17.1	0.11	2.4E-4	42	0.053	2.3	0.44	0.0141	0.64	90.0	0.6	153	90	n.d.	n.d.

^aActivity ratios and ages calculated using decay constants: λ²³⁸U 1.55125E-10, λ²³²Th 4.94752E-11 [Steiger and Jäger, 1977]. Ages calculated using Isoplot v. 3.76, with common Pb derived from Stacey and Kramers [1975] evolution model. Not determined = n.d.

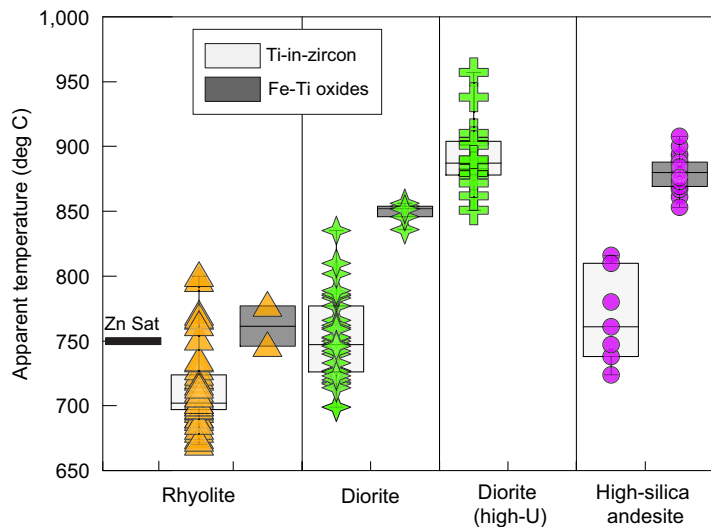


Figure 11. Box plot showing apparent temperatures for Augustine samples calculated from Ti-in-zircon and coexisting Fe-Ti oxide pairs. Boxes extend one quartile above and below the median for each population, which is shown by a solid line. Ti-in-zircon temperatures calculated using $\alpha\text{TiO}_2 = 0.85$ for rhyolite and 0.75 for diorite and andesite.

2013]. More detailed investigation into mineral compositions in the rhyolite may further constrain the proportion of antecrysts to phenocrysts within the rhyolite and thus provide insights into the mechanics of melt extraction.

6. Concluding Remarks

Here we show a temporal and geochemical link between two rock types at Augustine Volcano: crystal-poor rhyolite, erupted in the late Pleistocene, and dioritic blocks ejected in 2006. The overlap in zircon ages, as well as the trace-element patterns consistent with mineral-melt partitioning, strongly suggest that these rocks represent the extraction and eruption of melt from a crystal-rich magma body. Early Holocene andesitic to dacitic tephras may represent the crystal-rich intermediates from which the former two were separated. Further investigations of the early Holocene tephras may test this hypothesis.

Processes recorded by the rhyolite-diorite-dacite array are exceptional at this volcano. Holocene explosive eruptions instead produced high-silica andesites with 30–40 vol. % phenocrysts [Tappen *et al.*, 2009], and historical eruptions of lesser explosivity have erupted similar magmas [Johnston, 1978; Roman *et al.*, 2005;

subequal Zr concentrations in the rhyolite and dioritic blocks (70–105 ppm; Figure 2). The rhyolite also contains phenocrysts of quartz, orthopyroxene, plagioclase, and cummingtonite, some or all of which likely crystallized after the rhyolite was separated from the dioritic residue (Figure 13). Cummingtonite is stable at low temperatures (<800°C), high water contents, and high $f\text{O}_2$ [Geschwind and Rutherford, 1992]. This phase has not been identified in the dioritic inclusions, which contain magnesiohornblende with 9–10 wt % Al_2O_3 [De Angelis et al., 2013]. The rhyolite also contains high-Al hornblende [Nadeau et al.,

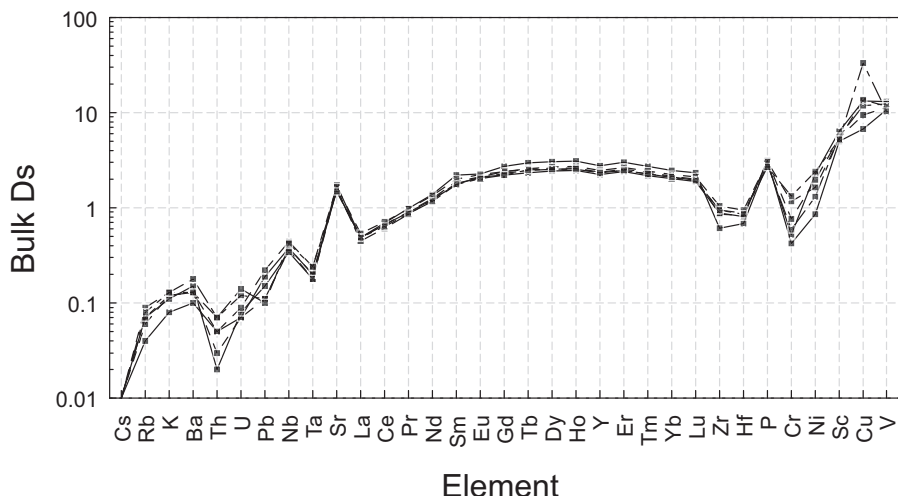


Figure 12. Calculated bulk partition coefficients for dioritic blocks ($n = 6$). See text for discussion.

Table 5. Bulk Trace-Element Partition Coefficients for Diorite Mineral Assemblage Calculated Using Rhyolite and Diorite Compositions^a

	12a	13a	27a	42a	27c	304a
K	0.08	0.12	0.12	0.11	0.13	0.13
P	2.98	3.08	2.83	3.14	3.03	2.69
La	0.49	0.49	0.45	0.49	0.54	0.49
Ce	0.69	0.66	0.61	0.66	0.71	0.64
Pr	0.99	0.90	0.86	0.89	0.97	0.87
Nd	1.38	1.25	1.21	1.22	1.34	1.17
Sm	2.19	1.90	1.82	1.76	2.00	1.76
Eu	2.26	2.11	2.05	2.11	2.24	2.02
Gd	2.71	2.40	2.29	2.19	2.41	2.20
Tb	2.96	2.52	2.45	2.33	2.59	2.50
Dy	3.05	2.61	2.55	2.43	2.69	2.52
Ho	3.09	2.62	2.52	2.45	2.73	2.56
Er	3.00	2.55	2.47	2.41	2.63	2.48
Tm	2.73	2.36	2.28	2.18	2.42	2.27
Yb	2.48	2.13	2.08	2.02	2.24	2.11
Lu	2.32	1.99	1.92	1.88	2.10	1.94
Ba	0.10	0.13	0.13	0.15	0.13	0.18
Th	0.05	0.03	0.07	0.02	0.05	0.07
Nb	0.38	0.36	0.38	0.34	0.44	0.42
Y	2.75	2.38	2.32	2.23	2.47	2.34
Hf	0.68	0.83	0.88	0.81	0.95	0.86
Ta	0.20	0.18	0.20	0.18	0.24	0.24
U	0.07	0.07	0.12	0.08	0.09	0.14
Pb	0.19	0.11	0.11	0.15	0.22	0.10
Rb	0.04	0.06	0.07	0.07	0.09	0.08
Cs	0.0010	0.0010	0.0010	0.0010	0.0010	0.0010
Sr	1.51	1.56	1.58	1.73	1.66	1.49
Sc	6.35	5.47	5.58	4.99	5.32	5.21
Zr	0.61	0.86	0.95	0.88	1.05	0.94
Ni	2.28	1.98	1.31	0.86	1.65	2.41
Cr	0.52	0.77	0.59	0.42	1.17	1.32
V	13.06	11.25	12.35	10.65	11.59	10.26
Cu	13.24	9.38	11.85	6.73	13.69	33.18
Zn	2.41	2.09	2.18	2.01	2.14	2.00
Calculated melt fraction	0.37	0.34	0.36	0.36	0.37	0.33

^aBulk partition coefficients calculated by dividing melt-free trace-element composition of each diorite sample by average rhyolite trace element composition. Melt fractions were calculated by assuming DCs = 0.001.

Larsen *et al.*, 2010]. These more recent magmas have rhyolitic melt phases that could potentially be extracted under the right conditions. For this to occur, however, would require the presence of a sufficiently large intermediate-composition magma body. We speculate that accumulation of a large volume dacitic mush may have been facilitated by ice cover over the volcano during the last ice age. Retreat of the ice cover decreased pressure and led to more voluminous eruptions in the early Holocene [e.g., Sigvaldason *et al.*, 1992; Huybers and Langmuir, 2009]. During the past few thousand years, lower overlying stress has allowed for less magma accumulation in the crust leading to more modest eruptions.

Table 6. Bulk REE Partition Coefficients for Diorite Mineral Assemblage Calculated Using Diorite Norm and Published Mineral Partition Coefficients^a

Sample 12a	Plagioclase	Clino-pyroxene	Ortho-pyroxene	Opaque	Amphibole	Apatite	Nonglass total	Bulk D From Mode	Bulk D (Melt-Free Diorite/Average Rhyolite)
Modal %	64.5	1.8	2.9	3.3	9.5		82.0		
Modal % Glass-free	78.6	2.2	3.5	4.0	11.6	0.6	100		
<i>Published Mineral Ds</i>									
La	0.3	1	0.4	0.66	0.86	35		0.60	0.49
Ce	0.22	1.5	0.46	0.71	2.13	47		0.77	0.69
Nd	0.19	3	0.6	0.93	5.19	64		1.24	1.38
Sm	0.12	3	0.78	1.2	7.76	80		1.60	2.19
Dy	0.14	4	0.52	4.4	10.20	90		2.09	3.05
Er	0.12	3	0.85	2	6.9	167		2.03	3
Yb	0.1	3	0.48	0.44	4.4	178		1.71	2.48

^aMode from Larsen *et al.* [2010]. Apatite estimated using norm calculator. Plagioclase Ds from Bacon and Druitt [1998]. Pyroxene Ds from Sisson [1991] and Bacon and Druitt [1988]. Magnetite Ds from Bacon and Druitt [1998] and Nash and Crecraft [1985]; Er was extrapolated. Amphibole Ds from Sisson [1994] using his sample DM-B. Apatite Ds from Brophy *et al.* [2011].

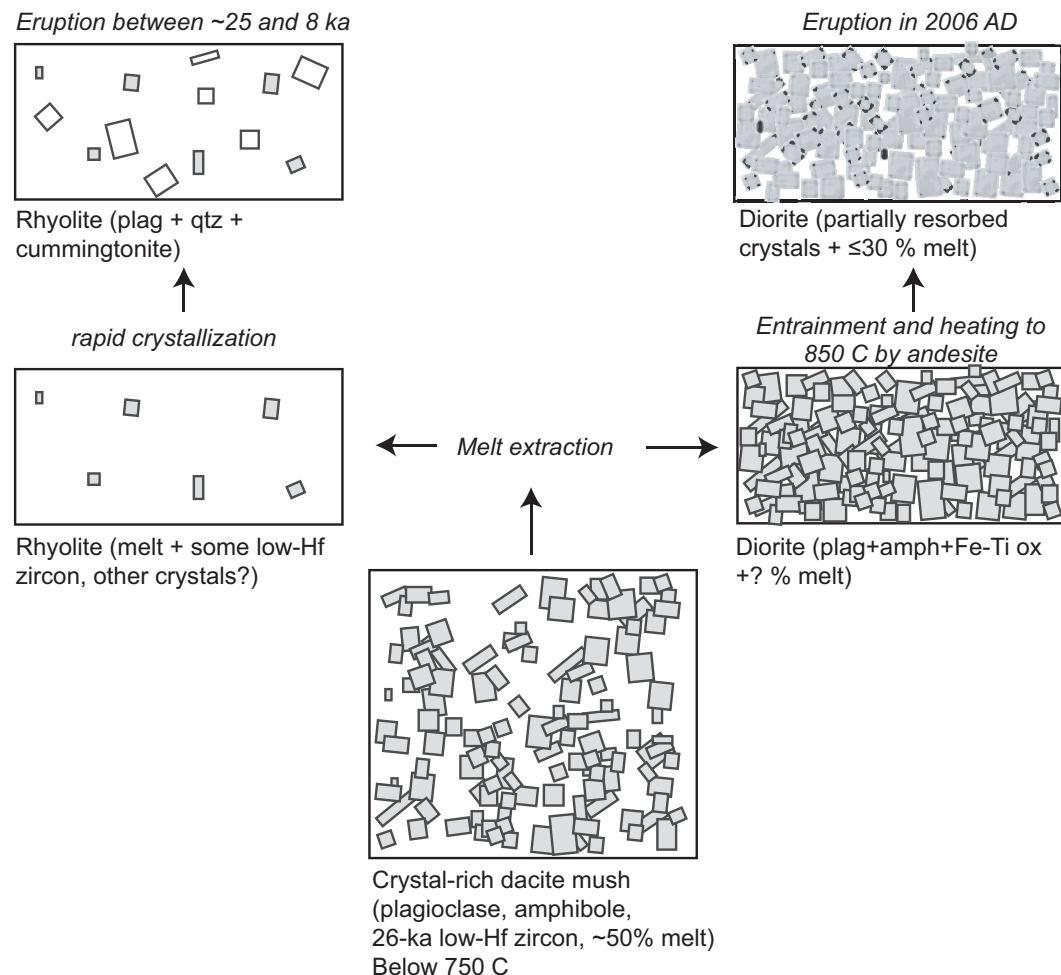


Figure 13. Cartoon highlighting stages in the formation of Augustine rhyolite magma and dioritic inclusions.

Acknowledgments

This work was supported by the Volcano Hazards Program of the U.S. Geological Survey. We thank Charlie Bacon and Chris Nye for constructive discussions, and Chris generously provided samples of the rhyolite. We are grateful to Heather Bleick and Leslie Hayden for electron probe analyses of Fe-Ti oxides, Marsha Lidzbarski for her expertise in separating and mounting zircon, and Mark Stelten and Kari Cooper for ICPMS U and Th isotope analyses. Tom Sisson provided insightful comments on an earlier version of the manuscript. We thank Axel Schmitt and Olivier Bachmann for their careful reviews. All data used to create figures in the manuscript can be found in Tables 1–5, or in supporting information Tables S2–S5.

References

- Arculus, R. J., and K. J. A. Wills (1980), The petrology of plutonic blocks and inclusions from the Lesser Antilles Island Arc, *J. Petrol.*, **21**, 743–799.
- Bachmann, O., and G. W. Bergantz (2004), On the origin of crystal-poor rhyolites: Extracted from batholithic crystal mushes, *J. Petrol.*, **45**, 1565–1582.
- Bachmann, O., and G. W. Bergantz (2008), Rhyolites and their source mushes across tectonic settings, *J. Petrol.*, **49**, 2277–2285.
- Bacon, C. R. (1986), Magmatic inclusions in silicic and intermediate volcanic rocks, *J. Geophys. Res.*, **91**, 6091–6112.
- Bacon, C. R., and T. H. Druitt (1988), Compositional evolution of the zoned calc-alkaline magma chamber of Mount Mazama, Crater Lake, Oregon, *Contrib. Mineral. Petrol.*, **98**, 224–256.
- Bacon, C. R., H. M. Persing, J. L. Wooden, and T. R. Ireland (2000), Late Pleistocene granodiorite beneath Crater Lake caldera, Oregon, dated by ion microprobe, *Geology*, **28**, 467–470.
- Bacon, C. R., T. W. Sisson, and F. K. Mazdab (2007), Young cumulate complex beneath Veniaminof caldera, Aleutian arc, dated by zircon in erupted plutonic blocks, *Geology*, **35**, 491–494.
- Bacon, C. R., J. A. Vazquez, and J. L. Wooden (2011), Peninsular terrane basement ages recorded by Paleozoic and Paleoproterozoic zircon in gabbro xenoliths and andesite from Redoubt volcano, Alaska, *Geol. Soc. Am. Bull.*, **124**, 24–34.
- Barth, A. P., and J. L. Wooden (2010), Coupled elemental and isotopic analyses of polygenetic zircons from granitic rocks by ion microprobe, with implications for melt evolution and the sources of granitic magmas, *Chem. Geol.*, **277**, 149–159.
- Bégét, J. E., and J. Kienle (1992), Cyclic formation of debris avalanches at Mount St Augustine volcano, *Nature*, **356**(6371), 701–704.
- Black, L. P., et al. (2004), Improved $^{206}\text{Pb}/^{238}\text{U}$ microprobe geochronology by the monitoring of a trace-element-related matrix effect; SHRIMP, ID-TIMS, ELA-ICP-MS and oxygen isotope documentation for a series of zircon standards, *Chem. Geol.*, **205**, 115–140.
- Brophy, J. G., T. Ota, T. Kunihiro, T. Tsujimori, and E. Nakamura (2011), In situ ion-microprobe determination of trace element partition coefficients for hornblende, plagioclase, orthopyroxene, and apatite in equilibrium with natural rhyolitic glass, Little Glass Mountain Rhyolite, California, *Am. Mineral.*, **96**, 1838–1850.

- Cervelli, P. F., T. Fournier, J. T. Freymueller, J. Power, M. Lisowski, and B. A. Pauk (2010), Geodetic constraints on magma movement and withdrawal during the 2006 eruption of Augustine Volcano, in *The 2006 Eruptions of Augustine Volcano, U.S. Geol. Surv. Prof. Pap. 1769*, edited by J. Power, M. L. Coombs, and J. Freymueller, pp. 427–452, U.S. Geol. Surv., Reston, Va.
- Cheng, H., R. L. Edwards, J. Hoff, C. D. Gallup, D. A. Richards, and Y. Asmerom (2000), The half-lives of uranium-234 and thorium 230, *Chem. Geol.*, 169, 17–33.
- Claiborne, L. L., C. F. Miller, B. A. Walker, J. L. Wooden, F. K. Mazdab, and F. Bea (2006), Tracking magmatic processes through Zr/Hf ratios in rocks and Hf and Ti zoning in zircons: An example from the Spirit Mountain batholith, Nevada, *Mineral. Mag.*, 70, 517–543.
- Coombs, M. L., K. V. Bull, J. Vallance, D. J. Schneider, E. E. Thoms, R. Wessels, and R. G. McGimsey (2010), Timing, distribution, and volume of proximal products of the 2006 eruption of Augustine Volcano, in *The 2006 Eruption of Augustine Volcano, Alaska, U.S. Geol. Surv. Prof. Pap. 1769*, edited by J. A. Power, M. L. Coombs, and J. T. Freymueller, pp. 145–186, U.S. Geol. Surv., Reston, Va.
- Daley, E. E. (1986), Petrology, geochemistry, and the evolution of magmas from Augustine Volcano, Alaska, MS thesis, Dep. of Geol. Geophys., Univ. of Alaska, Fairbanks.
- Davidson, J., S. Turner, and T. Plank (2013), Dy/Dy*: Variations arising from mantle sources and petrogenetic processes, *J. Petrol.*, 54(3), 525–537.
- De Angelis, S. H., J. Larsen, and M. Coombs (2013), Pre-eruptive magmatic conditions at Augustine Volcano, Alaska, 2006: Evidence from amphibole geochemistry and textures, *J. Petrol.*, 54, 1939–1961.
- Deering, C. D., and O. Bachmann (2010), Trace element indicators of crystal accumulation in silicic igneous rocks, *Earth Planet. Sci. Lett.*, 297, 324–331.
- Deering, C. D., O. Bachmann, and T. A. Vogel (2011), The Ammonia Tanks Tuff: Erupting a melt-rich rhyolite cap and its remobilized crystal cumulate, *Earth Planet. Sci. Lett.*, 310, 518–525.
- Dufek, J., and O. Bachmann (2010), Quantum magmatism: Magmatic compositional gaps generated by melt-crystal dynamics, *Geology*, 38, 687–690.
- Ferry, J. M., and E. B. Watson (2007), New thermodynamic models and revised calibrations for the Ti-in-zircon and Zr-in-rutile thermometers, *Contrib. Mineral. Petrol.*, 154, 429–437.
- Gelman, S. E., C. D. Deering, O. Bachmann, C. Huber, and F. J. Gutierrez (2014), Identifying crystal graveyards remaining after large silicic eruptions, *Earth Planet. Sci. Lett.*, 403, 299–306.
- Geschwind, C.-H., and M. J. Rutherford (1992), Cummingtonite and the evolution of the Mount St. Helens (Washington) magma system: AN experimental study, *Geology*, 20, 1011–1014.
- Ghiorso, M. S., and B. W. Evans (2008), Thermodynamics of rhombohedral oxide solid solutions and a revision of the Fe-Ti two-oxide geothermometer and oxygen-barometer, *Am. J. Sci.*, 308, 957–1039.
- Glazner, A. F., D. S. Coleman, and J. M. Bartley (2008), The tenuous connection between high-silica rhyolites and granodiorite plutons, *Geology*, 36, 183–186.
- Hiess, J., A. P. Nutman, V. C. Bennett, and P. Holden (2008), Ti-in-zircon thermometry applied to contrasting Archean metamorphic and igneous systems, *Chem. Geol.*, 247, 323–338.
- Hoskin, P. W. O., and U. Schaltegger (2003), The composition of zircon and igneous and metamorphic petrogenesis, *Rev. Mineral. Geochem.*, 53, 27–55.
- Huybers, P., and C. Langmuir (2009), Feedback between deglaciation, volcanism, and atmospheric CO₂, *Earth Planet. Sci. Lett.*, 286, 479–491.
- Johnston, D. A. (1978), Volatiles, magma mixing, and the mechanism of eruption at Augustine Volcano, Alaska, PhD thesis, Univ. of Wash., Seattle.
- Larsen, J. F., C. J. Nye, M. L. Coombs, M. Tilman, P. Izbekov, and C. Cameron (2010), Petrology and geochemistry of the 2006 eruption of Augustine Volcano, in *The 2006 Eruption of Augustine Volcano, U.S. Geol. Surv. Prof. Pap. 1769*, edited by J. A. Power, M. L. Coombs, and J. T. Freymueller, pp. 335–382, U.S. Geol. Surv., Reston, Va.
- Ludwig, K. (2009), Isoplot v. 3.71: A geochronological Toolkit for Microsoft Excel, *Spec. Publ.*, 4, 70 p., Berkeley Geochronol. Cent., Berkeley, Calif.
- Ludwig, K. R. (2003), Isoplot 3.00: A geochronological toolkit for Microsoft Excel, *Spec. Publ.*, 4, Berkley Geochronol. Cent., Berkeley, Calif.
- Nadeau, P. A., J. D. Webster, C. W. Mandeville, B. A. Goldoff, N. Shimizu, and B. D. Monteleone (2013), A glimpse into Augustine Volcano's pre-glacial past: Insight from a massive rhyolite deposit, Abstract V21C-2749 presented at 2013 Fall Meeting, AGU, San Francisco, Calif.
- Nash, W. P., and H. R. Crecraft (1985), Partition coefficients for trace elements in silicic magmas, *Geochim. Cosmochim. Acta*, 49, 2309–2322.
- Nye, C. J., and D. L. Turner (1990), Petrology, geochemistry, and age of the Spur volcanic complex, eastern Aleutian arc, *Bull. Volcanol.*, 52(3), 205–226.
- Paces, J. B., and J. D. Miller (1993), U-Pb ages of Duluth complex and related mafic intrusions, northeastern Minnesota: Geochronological insights to physical, petrogenetic, paleomagnetic, and tectonomagmatic processes associated with the 1.1 Ga mid-continent rift system, *J. Geophys. Res.*, 98, 13,997–14,013.
- Reid, M., C. Coath, T. M. Harrison, and K. McKeegan (1997), Prolonged residence times for the youngest rhyolites associated with Long Valley Caldera: Th-230-U-238 ion microprobe dating of young zircons, *Earth Planet. Sci. Lett.*, 150, 27–39.
- Reid, M. R., J. A. Vazquez, and A. K. Schmitt (2011), Zircon-scale insights into the history of a supervolcano, Bishop Tuff, Long Valley, California, with implications for the Ti-in-zircon geothermometer, *Contrib. Mineral. Petrol.*, 161, 293–311.
- Reubi, O., and J. Blundy (2009), A dearth of intermediate melts at subduction zone volcanoes and the petrogenesis of arc andesites, *Nature*, 461, 1269–1273.
- Roman, D. C., K. V. Cashman, C. A. Gardner, P. Wallace, and J. Donovan (2005), Storage and interaction of compositionally heterogeneous magmas from the 1986 eruption of Augustine Volcano, Alaska, *Bull. Volcanol.*, 68, 240–254.
- Cambridge, M. S., and W. Compston (1994), Mixture modeling of multi-component data sets with application to ion-probe zircon ages, *Earth Planet. Sci. Lett.*, 128, 373–390.
- Schmitt, A. K. (2006), Laacher See revisited: High-spatial-resolution zircon dating indicates rapid formation of a zoned magma chamber, *Geology*, 34, 597–600.
- Siebert, L., J. E. Begét, and H. Glicken (1995), The 1883 and late-prehistoric eruptions of Augustine volcano, Alaska, *J. Volcanol. Geotherm. Res.*, 66, 367–395.
- Sigvaldason, G. E., K. Annertz, and M. Nilsson (1992), Effect of glacier loading/unloading on volcanism: Postglacial volcanic production rate of the Dyngjufjöll area, central Iceland, *Bull. Volcanol.*, 54, 385–392.
- Sisson, T. W. (1991), Pyroxene-high silica rhyolite trace element partition coefficients measured by ion microprobe, *Geochim. Cosmochim. Acta*, 55, 1575–1585.

- Sisson, T. W. (1994), Hornblende-melt trace-element partitioning measured by ion microprobe, *Chem. Geol.*, 117, 331–344.
- Sisson, T. W., and C. R. Bacon (1999), Gas-driven filter pressing in magmas, *Geology*, 27, 613–616.
- Stacey, J. T., and J. D. Kramers (1975), Approximation of terrestrial lead isotope evolution by a two-stage model, *Earth Planet. Sci. Lett.*, 26, 207–221.
- Steiger, R., and E. Jäger (1977), Subcommission on geochronology: Convention on the use of decay constants in geo- and cosmochronology, *Earth Planet. Sci. Lett.*, 36, 359–362.
- Steiner, A., B. L. Browne, and C. J. Nye (2012), Quenched mafic inclusions in ≤ 2200 yrs B.P. deposits at Augustine Volcano, Alaska, *Int. Geol. Rev.*, 54(11), 1241–1270.
- Stelten, M. E., and K. M. Cooper (2012), Constraints on the nature of the subvolcanic reservoir at South Sister volcano, Oregon from U-series dating combined with sub-crystal trace-element analysis of plagioclase and zircon, *Earth Planet. Sci. Lett.*, 313–314, 1–11.
- Streckeisen, A. (1976), To each plutonic rock its proper name, *Earth Sci. Rev.*, 12, 1–33.
- Tappa, M. J., D. S. Coleman, R. D. Mills, and K. M. Samperton (2011), The plutonic record of a silicic ignimbrite from the Latir volcanic field, New Mexico, *Geochem. Geophys. Geosyst.*, 12, Q10011, doi:10.1029/2011GC003700.
- Tappen, C. M., J. D. Webster, C. W. Mandeville, and D. Roderick (2009), Petrology and geochemistry of ca. 2100–1000 a.B.P. magmas of Augustine volcano, Alaska, based on analysis of prehistoric pumiceous tephra, *J. Volcanol. Geotherm. Res.*, 183, 42–62.
- Thompson, J. A. (2011), Uranium series analysis of 2006 Augustine volcanics: An investigation into the timescales of magmatic processes, MS thesis, Univ. of Iowa, Iowa.
- Till, A. B., M. E. Yount, and M. L. Bevier (1994), The geologic history of Redoubt Volcano, Alaska, *J. Volcanol. Geotherm. Res.*, 62(1), 11–30.
- Vazquez, J. A., P. J. Shamberger, and J. E. Hammer (2007), Plutonic xenoliths reveal the timing of magma evolution at Hualalai and Mauna Kea, Hawaii, *Geology*, 35, 695–698.
- Waitt, R. B., and J. E. Begét (2009), Volcanic processes and geology of Augustine Volcano, Alaska, *U.S. Geol. Surv. Prof. Pap.* 1762, 78 p.
- Wallace, K., and M. L. Coombs (2013), Constructing a reference tephrochronology for Augustine Volcano, Alaska, Abstract V23C-2839 presented at 2013 Fall Meeting, AGU, San Fransico, Calif.
- Webster, J. D., C. W. Mandeville, B. Goldoff, M. L. Coombs, and C. Tappen (2010), Augustine Volcano, Alaska: The influence of volatile components in magmas erupted AD 2006 to 2100 years before present, in *The 2006 Eruption of Augustine Volcano, U.S. Geol. Surv. Prof. Pap. 1769*, edited by J. A. Power, M. L. Coombs, and J. T. Freymueller, pp. 383–423, U.S. Geol. Surv., Reston, Va.
- Wiedenbeck, M., et al. (2004), Further characterization of the 91500 zircon crystal, *Geostand. Geanal. Res.*, 28, 9–39.
- Zimmer, M. M., T. Plank, E. H. Hauri, G. M. Yogodzinski, P. Stelling, J. F. Larsen, B. S. Singer, B. R. Jicha, C. W. Mandeville, and C. J. Nye (2010), The role of water in generating the calc-alkaline trend: New volatile data for Aleutian magmas and a new tholeiitic index, *J. Petrol.*, 51(12), 2411–2444.